



School of Chemistry

# **The use of Optical Emission Spectroscopy to probe microwave-activated silicon-containing hydrogen plasmas**

Alim Lalji

**This thesis is submitted in partial fulfilment of the requirements for the  
Honours Degree of MSci at the University of Bristol**

Submitted: April 2018

Supervisor: Professor M. N. R. Ashfold

Second Assessor: Professor P.W. May

Section: Physical and Theoretical

# Abstract

Optical Emission Spectroscopy was used to observe H $\gamma$ , Si\* ( $^1P^o_1 \rightarrow ^1S_0$ ) and SiH (A-X) emissions in two different microwave plasma gas mixtures. For the first system explored, a 0.1% SiH $_4$  in H $_2$  gas mixture was fed into a microwave-activated H $_2$  plasma, henceforth referred to as the SiH $_4$ /H $_2$  plasma. The emissions were observed as a function of the flow rate of the 0.1% SiH $_4$  in H $_2$  mixture,  $F(\text{SiH}_4)$ , applied microwave power,  $P$ , and total pressure,  $p$ . The second system studied was a H $_2$ /Ar gas mixture with a 0.7 mm Si wafer present. In this case, the argon flow rate,  $F(\text{Ar})$  was the only parameter varied.

From the emission spectroscopy data obtained, computational programs MATLAB and PGOPHER were implemented to de-skew and model diatomic emissions respectively. Together, the use of these programs meant that emission spatial distributions for each species could be determined. A spatial distribution is a plot of the relative emission intensity of a species, as a function of height above the substrate surface,  $z$ . In this way, the behaviour of these excited state species were illustrated, as a function of the parameters discussed.

The spatial distributions illustrated that H\*, Si\* and SiH\* species were prominent, particular in the core of the plasma. In the SiH $_4$ /H $_2$  plasma, Si\* and SiH\* were observed throughout. They also appeared to have similar trends in their spatial profiles, regardless of the parameter being varied. With respect to the H $_2$ /Ar system, Si\* and SiH\* were only observed following etching of the OH terminated layer of the Si substrate. On comparing Si\* and SiH\* spatial profiles in the two different silicon-containing hydrogen plasmas, differences in their trends were observed, a feature which can be attributed to the different sources of silicon.

SEM was an additional technique used in the study, in order to examine the surface topography of the Si wafer, before and after exposure to the H $_2$ /Ar.

# Acknowledgements

Firstly I would like to express my sincere thanks to my supervisor, Professor Mike Ashfold. His door has always been open to me and through our discussions, he has always pointed me in the right direction. A special thank you to Ed Mahoney for his constant support and encouragement, both in and out of the lab. Also, thank to Dr Sohail Mushtaq for helping me to prepare for my project presentation. The three of them have definitely made me feel a part of the team, for which I am grateful.

Secondly, I would like to extend my gratitude to Professor Paul May for his helpful insight and suggestions in tackling the project. Additionally, I would like to acknowledge my personal tutor, Professor Charl Faul for all his support and advice during my time at Bristol.

I would like to also thank Dr Robert Harniman and Dr Jean-Charles Eloi for their time and help with the microscopy imaging of the Si wafers. Additionally, I would like to say a big thank you to both the Bristol CVD diamond group and the LASER group for making this a truly enjoyable experience.

Finally, I would like to say big thank you to my parents, Karim and Ama, as well as my brother, Zahid. It's been a tough few years for us all, myself included. Your belief and confidence in me have helped me to push through. I hope I can make you guys proud this year.

# Contents

Abstract .....	2
Acknowledgements.....	3
List of Figures .....	7
1. Introduction.....	10
1.1 Diamond and its Properties .....	10
1.2 History of Synthetic Diamond Formation .....	13
1.2.1 HPHT .....	13
1.2.2 Chemical Vapour Deposition, CVD.....	13
1.2.3 Microwave Plasma Chemical Vapour Deposition, MWPCVD .....	15
1.3 Reactions within the MWPCVD reactor .....	16
1.3.1 Hydrogen Chemistry and its Importance.....	16
1.3.2 Carbon Chemistry .....	18
1.3.3 Regions of the reactor .....	21
1.3.4 Addition of carbon unit to growing film.....	24
1.4 Silicon Doped Diamond.....	26
1.4.1 Silicon-Vacancy Defect.....	26
1.4.2 Formation of silicon doped diamond .....	27
1.5 Optical Emission Spectroscopy.....	28
1.6 Aims.....	29
1.7 References .....	29
2. Experimental .....	31
2.1 Microwave Plasma CVD reactor .....	31

2.1.1 MWPCVD reactor .....	31
2.1.2 SiH <sub>4</sub> /H <sub>2</sub> plasma .....	34
2.1.3 Si substrate present in H <sub>2</sub> /Ar.....	35
2.2 Optical Emission Spectrometry .....	36
2.2.1 Andor Shamrock 500i Spectrograph .....	36
2.2.2 Andor Newton 970 CCD detector.....	37
2.2.3 Specific Emissions Observed.....	38
2.3 Computational Programs .....	39
2.4 Scanning Electron Microscopy, SEM .....	40
2.5 References .....	42
3. Results and Discussion .....	43
3.1 OES spectrum .....	43
3.2 PGOPHER Fit.....	46
3.3 SiH <sub>4</sub> /H <sub>2</sub> mixture .....	48
3.3.1 Spatial distributions for H*, Si* and SiH* as a function of <i>P</i> and as a function of <i>p</i> .....	49
3.3.2 Spatial distributions for H*, Si* and SiH* as a function of <i>F</i> (SiH <sub>4</sub> )	53
3.4 Si substrate in the presence of a H <sub>2</sub> /Ar mixture .....	56
3.4.1 Etching process .....	56
3.4.2 Spatial distributions for H*, Si* and SiH* as a function of <i>F</i> (Ar)....	58
3.4.3 SEM.....	60
3.5 Comparison of spatial distributions for <i>I</i> (H*), <i>I</i> (Si*) and <i>I</i> (SiH*) from a Si wafer in a pure H <sub>2</sub> plasma and those from a SiH <sub>4</sub> /H <sub>2</sub> .....	62
3.6 Gas phase chemistry.....	65

3.7	References .....	66
4.	Conclusion .....	67
5.	Future Work .....	68
5.1	Modelling of the silicon-containing hydrogen plasmas .....	68
5.2	Cavity Ring Down Spectroscopy Study .....	68
5.3	An OES study of a CH <sub>4</sub> /SiH <sub>4</sub> /H <sub>2</sub> plasma .....	69
5.4	References .....	69

# List of Figures

Figure 1.1: Illustrations of the structures of (a) diamond and (b) graphite. <sup>4</sup> .....	11
Figure 1.2: Simplified carbon phase diagram illustrating the effect of pressure and temperature in determining the predominant carbon form, such as between graphite and diamond. <sup>5</sup> .....	12
Figure 1.3: Schematic diagrams of the (a) NIRIM type and (b) ASTEX type MWPCVD reactors. <sup>1</sup> .....	15
Figure 1.4: Bachmann Triangle which illustrates the elemental C:H:O ratios needed for diamond growth to occur. <sup>17</sup> .....	18
Figure 1.5: 2D (r, z) plot of a modelled 4.4% CH <sub>4</sub> /7% Ar/ H <sub>2</sub> plasma, illustrating the variation of $T_{\text{gas}}$ , in Kelvin, with respect to position, r, within the reactor and height about the substrate, z. <sup>15</sup> .....	21
Figure 1.6: 2D (r,z) plots of a modelled 4.4% CH <sub>4</sub> /7% Ar/ H <sub>2</sub> plasma, illustrating the variation in the mole fractions of: (a) C <sub>2</sub> H <sub>2</sub> , $X(\text{C}_2\text{H}_2)$ and (b) CH <sub>4</sub> , $X(\text{CH}_4)$ . Note that the values in (b) have been converted into % values, unlike those in (a). <sup>12</sup> .....	23
Figure 1.7: C <sub>2</sub> H <sub>4</sub> bridged species .....	25
Figure 1.8: Schematic of a Silicon-Vacancy centre in CVD diamond. <sup>21</sup> .....	26
Figure 2.12: The custom designed ASTEX type MWPCVD reactor used. The left half schematically shows the reactor's components. <sup>1</sup> .....	31
Figure 2.2: Images of the (a) 2 kW, 2.45 GHz Muegge power supply and generator, (b) Gas cylinders of the feed gases and (c) Central system which controlled the individual mass flow controllers .....	32-33
Figure 2.33: Schematic diagram of the Czerny-Turner monochromator <sup>5</sup> .....	36
Figure 2.4: Top down view of the Andor Shamrock 500i Spectrograph .....	37
Figure 2.5: Simulated spectrum for SiH (A-X), generated by PGOPHER .....	39
Figure 2.6: An image of the JEOL IT300 Scanning Electron Microscope used in this study. <sup>13</sup> .....	40

Figure 2.7: The two Si substrates imaged by SEM: (a) Si wafer exposed to the H <sub>2</sub> /Ar plasma and (b) Clean, unexposed Si wafer.....	<b>41</b>
Figure 3.14: Example of OES spectrum collected. This particular spectrum corresponds to SiH <sub>4</sub> /H <sub>2</sub> plasma, at $P= 0.9$ kW, with all other parameters at 'base conditions' .....	<b>43</b>
Figure 3.2: False colour plot indicating intensity as a function of wavelength (x-axis) and height (y-axis). The plot shown here corresponds to the SiH <sub>4</sub> /H <sub>2</sub> plasma, at $P= 0.9$ kW, with all other parameters at 'base conditions' .....	<b>45</b>
Figure 3.3: PGOPHER Fitting process of SiH (A-X) in a SiH <sub>4</sub> /H <sub>2</sub> plasma, corresponding to $P= 0.9$ kW, $z = 9.75 \pm 0.75$ mm. The red spectrum corresponds to the experimentally obtained spectrum. <sup>2</sup> .....	<b>46</b>
Figure 3.4: (a) PGOPHER Fit of SiH (A-X) in a SiH <sub>4</sub> /H <sub>2</sub> plasma, corresponding to $P= 0.9$ kW, $z = 9.75 \pm 0.75$ mm, (b) Residuals plot. <sup>2</sup> .....	<b>47</b>
Figure 3.5: Spatial profiles for H* in a SiH <sub>4</sub> /H <sub>2</sub> plasma, as a function of: (a) $P$ and (b) $p$ .....	<b>49</b>
Figure 3.6: Spatial profiles of Si* in a SiH <sub>4</sub> /H <sub>2</sub> plasma, as a function of: (a) $P$ and (b) $p$ . Also, spatial profiles of SiH* under the same plasma as a function of: (c) $P$ and (d) $p$ .....	<b>50</b>
Figure 5: Spatial profiles for (a) H*, (b) Si* and (c) SiH* as a function of $F(\text{SiH}_4)$ . Also, presented are plots showing the variation of (d) $I(\text{Si}^*)$ and (e) $I(\text{SiH}^*)$ with $F(\text{SiH}_4)$ , at $z = 13.5 \pm 1.5$ mm.....	<b>53-54</b>
Figure 3.8: Spatial profile for Si* as a function of $F(\text{Ar})$ , in a H <sub>2</sub> /Ar mixture with a Si substrate present. These spatial profiles correspond to the first run.....	<b>56</b>
Figure 3.9: Spatial profiles for (a) H*, (b) Si* and (c) SiH* as a function of $F(\text{Ar})$ , in a H <sub>2</sub> /Ar mixture with a Si substrate present. These spatial profiles correspond to the second run, and hence following the etching of the OH terminated layer.....	<b>58</b>
Figure 3.10: Representative SED type SEM images of the (a) Clean, unexposed Si wafer and (b) Si wafer having been exposed to a H <sub>2</sub> /Ar plasma. Both images were taken at a magnification of x1000.....	<b>60-61</b>

Figure 3.11 : Comparison of spatial profiles for (a)  $H^*$ , (b)  $Si^*$  and (c)  $SiH^*$  from a Si wafer in a pure  $H_2$  plasma (blue) and that arising from a  $SiH_4/H_2$  plasma operating at base conditions (black).....63

# 1. Introduction

## 1.1 Diamond and its Properties

Throughout history, there has been a fascination with natural diamond. Its extensive use in forming beautiful and precious gemstones has been marvelled at. However, its unique physical and mechanical properties have made it intriguing to scientists, particularly with respect to its potential scientific and engineering applications.

Diamond, along with graphite, is one of the most recognised allotropes of carbon. Although they share the same elemental composition, the two significantly differ in their properties. For example, diamond is extremely hard to the point that it is commonly used to form cutting tools, whereas graphite can serve as a lubricant due to its softness.<sup>1,2</sup> The extreme hardness is just one of several properties that are unique to diamond, as evident from Figure 1.1.

Property	Value
Mechanical Hardness / GPa	90 – 100
Bulk Modulus / N m <sup>-2</sup>	1.2 x 10 <sup>12</sup>
Optical Transparency	Deep UV to Far IR
Bandgap / eV	5.47
Thermal Expansion Coefficient / K <sup>-1</sup>	0.86 x 10 <sup>-6</sup>
Thermal Conductivity / W m <sup>-1</sup> K <sup>-1</sup>	2 x 10 <sup>3</sup>

**Table 1.1: Several key properties of diamond.<sup>1,3</sup>**

Although elemental composition is a major factor, it is the structure of diamond which gives rise to its unique properties and hence distinguishes it from graphite, as shown in Figure 1.1.

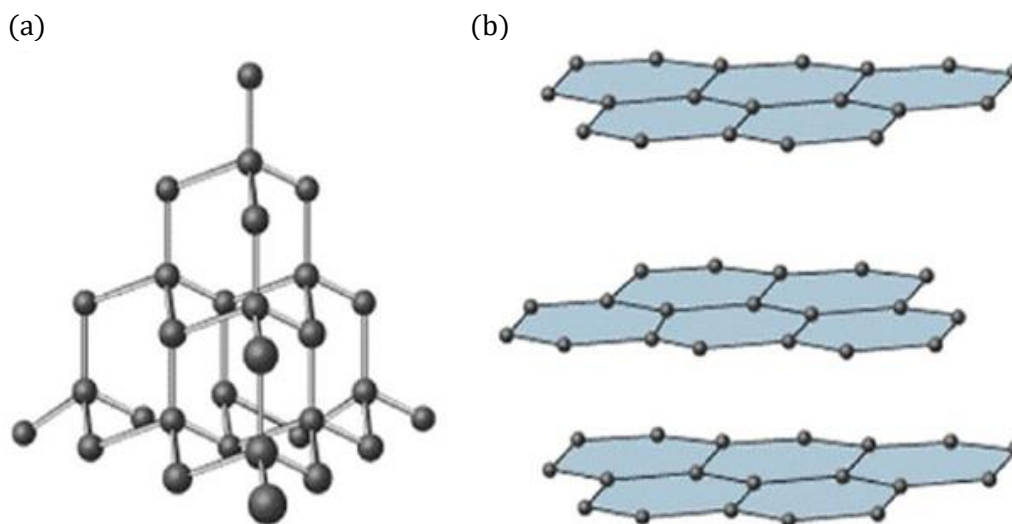


**Figure 6.1: Illustrations of the structures of (a) diamond and (b) graphite.<sup>4</sup>**

In graphite, each  $sp^2$  hybridised carbon atom is bonded to three neighbouring atoms, resulting in planar layers. These individual layers are strong since they are held together by strong covalent bonds and are additionally stabilised by delocalisation. However, these layers interact with one another through weak van der Waals' forces. These weak interactions allow for the layers to slide past each other, resulting in graphite's softness and hence use as a lubricant.<sup>2</sup> On the other hand, diamond is composed of  $sp^3$  hybridised carbon atoms in a tetrahedral network, with each carbon attached to four neighbours. Additionally, these short range, covalent carbon-carbon bonds are strong and hence difficult to break. Therefore, the observed properties in diamond are determined by two factors: its elemental composition and its structure. However, it is its unique structure which differentiates it from graphite, which has been found to demonstrate rather different properties.

In any discussion of diamond formation, it is necessary to consider graphite since a relationship exists between these two allotropes, as illustrated in Figure 1.2. At low pressures and temperatures, such as at room temperature and pressure, graphite is the more thermodynamically stable of the two carbon forms, with a large activation barrier preventing interconversion between the two. Under these conditions, diamond is a metastable species meaning that it can be obtained through kinetic control. This is the basis of Chemical Vapour Deposition, as discussed in Section 1.2.2. However, under high pressure and high temperature conditions, graphite is metastable with diamond being the more thermodynamically stable carbon allotrope.

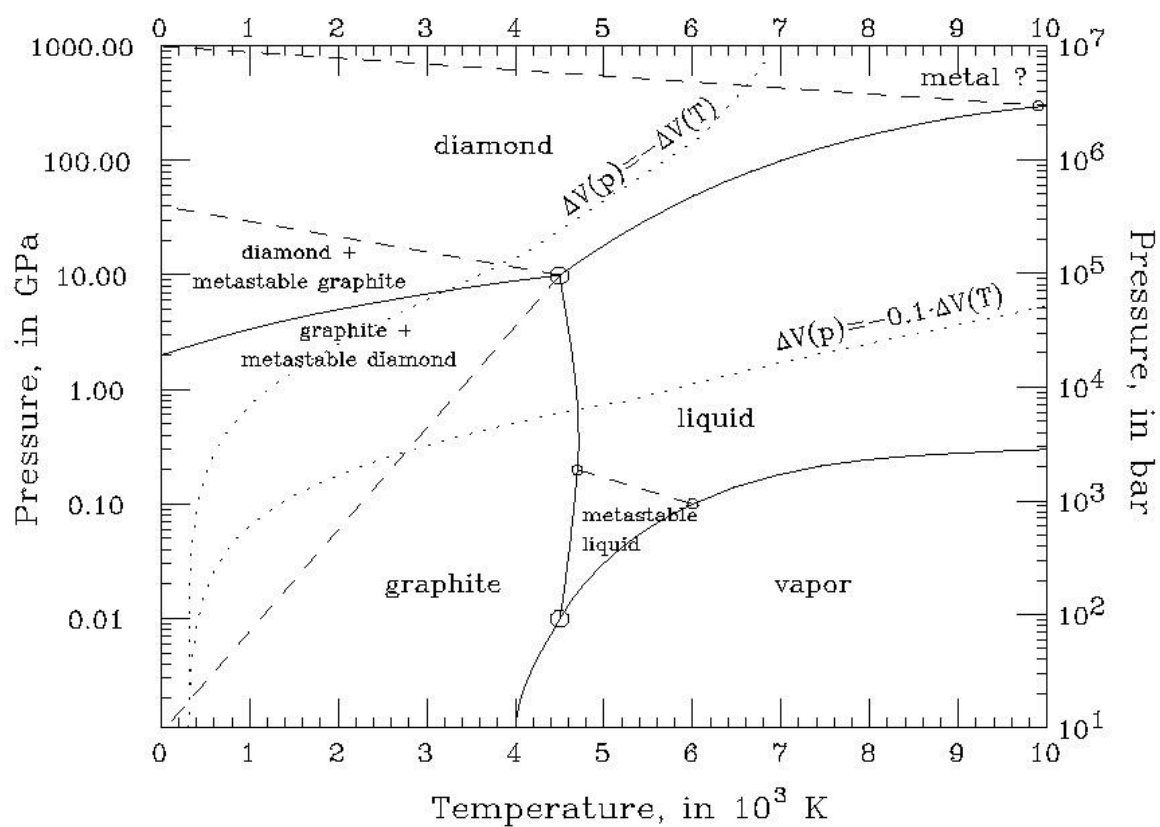


Figure 1.2: Simplified carbon phase diagram illustrating the effect of pressure and temperature in determining the predominant carbon form, such as between graphite and diamond.<sup>5</sup>

## 1.2 History of Synthetic Diamond Formation

### 1.2.1 HPHT

The first successful method for synthetic diamond formation was developed by General Electric in 1954. This process, known as the high-pressure high-temperature method, HPHT, mimicked natural diamond formation in the Earth, whereby carbon containing compounds are exposed to extreme pressures and temperatures. Thus, graphite, in the presence of a molten metal catalyst, is subjected to high pressure of 60 kbar (6 GPa) and temperatures over 2000 K, and left to crystallise as diamond.<sup>6</sup> In the HPHT method, the thermodynamics are exploited as under these extreme conditions, diamond is the more stable structure. The HPHT method was the first commercial success for the development of synthetic diamond, and since its inception it continues to be one of two main methods of synthetic diamond formation.

### 1.2.2 Chemical Vapour Deposition, CVD

An alternative to the HPHT method is known as Chemical Vapour Deposition, CVD. In contrast to HPHT, CVD diamond formation is carried out at lower pressures and temperatures.

Under such conditions, graphite is the more thermodynamically stable carbon allotrope, and as such the process cannot involve a direction transformation of graphite into diamond. Instead of using such extreme conditions, the CVD method involves the addition of individual carbon atoms to an appropriate surface. The nature of the surface affects the type of growth, with homoepitaxial growth occurring on diamond surfaces, whilst heteroepitaxial growth is conducted on non-diamond substrates. Regardless of the type of growth, the basis of the CVD process relies on the exploitation of the kinetic chemistry. Another factor aiding the CVD process is that it incorporates a method of removing graphitic carbon, something which would otherwise affect the purity and growth of the CVD diamond formed. Both of these factors are explained below, as reported by Eversole and Angus. In fact, since the late 1950s, there have been several key discoveries which have led to the development of the modern CVD method used today.

In 1958, William G. Eversole at the Union Carbide Corporation was the first to report growth of diamond at sub-atmospheric pressures. In his experiment, carbon-containing gases such as methane were passed over diamond seed crystals, resulting in the deposition of carbon in the form of diamond. The kinetics of this process were found to favour diamond formation over graphite, as the rate of deposition of carbon in the form of diamond was greater than the rate of deposition of graphitic carbon.<sup>7</sup>

However, although the experiment was a success with respect to diamond formation, graphitic carbon in the form of black carbon was a by-product of the process. This was an issue since it was found to not only affect the purity of the diamond grown but to also hinder the rate of growth. A solution to this process was reported by Angus et al. in 1968. It was found that graphite could be etched from the system by passing hydrogen gas over the diamond crystals. Through the use of this cleaning process, it was reported that 99% of the graphite had been removed, with only 0.22% of the diamond lost. The success of this process can be explained due to the vastly differing reaction rates of hydrogen with graphite and diamond respectively.<sup>8</sup>

Additionally, in 1981, work by Spitsyn et al. provided evidence for the possibility of diamond growth on non-diamond substrates.<sup>9</sup> Therefore, by the early 1980's, a relatively effective method for the growth of diamond on both diamond and non-diamond substrates had been devised. However, in 1982 and 1983, a Japanese research group at the National Institute for Research in Inorganic Materials, NIRIM, put forward two different methods of activating the gaseous hydrocarbon/hydrogen mixture. The result of this addition to the CVD process was found significantly enhance the growth rate, whilst still allowing the synthesis of good quality diamond film.<sup>1</sup>

In 1982, Matsumoto et al. put forward Hot Filament CVD, HFCVD. During this procedure, a CH<sub>4</sub>/H<sub>2</sub> mixture was passed into a heated reaction chamber, in which a hot tungsten filament was held in close proximity to the substrate.<sup>10</sup> The following year, the same group developed the first Microwave Plasma CVD reactor, MWPCVD, as reported by Kamo et al. In their study, a dilute, 1 - 3% CH<sub>4</sub> in H<sub>2</sub> mixture was passed into a quartz tube, into which microwave power had also been coupled, resulting in the formation of an induced glow discharge.<sup>11</sup>

Development of these activation methods by the NIRIM team led to further study in this area, resulting in alternative techniques such as DC plasma jets and combustion. However, the majority of study and growth of CVD diamond is carried out by one of HFCVD and MWPCVD processes.<sup>12</sup>

### 1.2.3 Microwave Plasma Chemical Vapour Deposition, MWPCVD

Although both serve as key methods of activation, there are several advantages to the use of a MWPCVD reactor. High powers can be generated in this type of reactor, resulting in higher diamond growth rates of  $> 10 \mu\text{m h}^{-1}$ , exceeding that of HFCVD reactors. These high powers also allow for gases with higher bond energies to be processed. This, together with the fact that MWPCVD reactors are not sensitive to any oxidising or corrosive gases, means that a much wider range of gas mixtures can be used in this type of system. Finally, the absence of a filament means that the system is cleaner since the diamond film cannot be contaminated with filament material.<sup>1</sup>

There are two types of MWPCVD reactor, both of which operate in similar fashions but differ in their set up, as shown in Figure 1.3. In the study reported here, an ASTEX type reactor was used, as shown in Figure 1.3 (b) and expanded on in Section 2.1.1. Essentially, microwaves are generated and fed in through the tuning antenna into the reactor. On passing through the quartz window, they interact with the input gas mixture which is fed directly into the lower half of the reactor. This interaction results in activation.

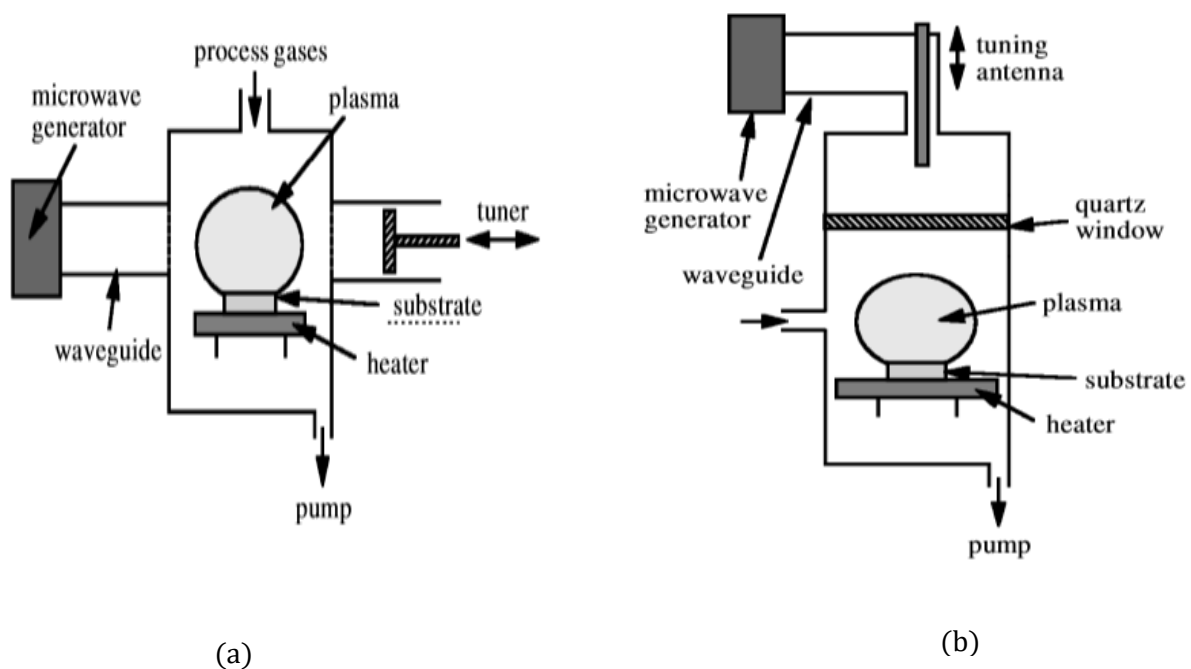


Figure 1.3: Schematic diagrams of the (a) NIRIM type and (b) ASTEX type MWPCVD reactors.<sup>1</sup>

The activation process is important in driving the gas phase chemistry for CVD diamond growth, as discussed in Section 1.3.

## 1.3 Reactions within the MWPCVD reactor

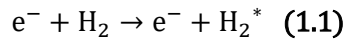
From the initial input of a hydrocarbon/H<sub>2</sub> gas mixture, to the adsorption and hence incorporation of a carbon unit into the growing diamond film, the CVD process is composed of a series of complex chemical and some physical processes, some of which are discussed in the following section.

Firstly, Section 1.3.1 goes into detail regarding the initial activation process, resulting in the formation of atomic hydrogen. Atomic hydrogen is key with respect to the overall CVD growth process. Secondly, in Section 1.3.2, the gas phase carbon chemistry is discussed, with a particular focus on the range of hydrocarbon species that form. Section 1.3.3 considers the impact of the temperature of the gas mixture,  $T_{\text{gas}}$ , on the gas kinetics and concentration of the species present. Finally, with a better understanding of the gas phase chemistry, put forward in Sections 1.3.1 to 1.3.3, Section 1.3.4 considers the growth process of the diamond itself.

### 1.3.1 Hydrogen Chemistry and its Importance

The activation process involves the interaction of the incoming microwave radiation with electrons present in the input gas mixture. In this way, the microwaves couple energy to the electrons, resulting in their acceleration. These electrons, having gained energy from this process, then collide with H<sub>2</sub> molecules. Following this collision, there are several pathways resulting in atomic hydrogen formation. The predominant mechanism for such a system is dependent on total pressure,  $p$  and  $T_{\text{gas}}$ . For this particular study, it is important to note that the two different gas mixtures studied were primarily kept at a high pressure,  $p$ , of 150 Torr.

Under such conditions, thermal dissociation is the main mechanism of generating atomic hydrogen. Therefore, as a result of these electron-H<sub>2</sub> collisions, the H<sub>2</sub> molecules are vibrationally excited to higher vibrational states, as indicated by H<sub>2</sub>\* in Reaction 1.1.



This process leads to an increase in  $T_{\text{gas}}$ , as well as causing some ionisation. Through ionisation, more electrons are generated, enabling more collisions with H<sub>2</sub> molecules and hence further gas heating. In this way, H<sub>2</sub> is dissociated into atomic hydrogen, as shown in Reaction 1.2. After several reactor-gas turn-over times, which is the time taken for the gas mixture to remove 50% of the original content, the system reaches a steady state with respect to electron concentration, atomic H concentration,  $T_{\text{gas}}$ , MW power in and conducted power out.<sup>2,12</sup>



An alternative pathway for atomic hydrogen formation, under CVD conditions is through electron impact dissociation. This involves the excitation of  $H_2$  molecules to excited triplet states which can then radiate to the repulsive  $b^3\Sigma_u^+$ . As a result of this transition,  $H_2$  dissociates into atomic H. <sup>12,13</sup> However, under conditions of high pressure and  $T_{gas}$ , the rate of thermal dissociation of  $H_2$  has been reported to be at least an order of magnitude greater than electron impact dissociation. <sup>14,15</sup>

Atomic hydrogen has several important functions with respect to the growth process. Firstly, it is a key component with respect to the carbon chemistry occurring in the reactor, as expanded upon in Section 1.3.2. As discussed, its presence drives the generation of  $CH_y$  and  $C_2H_z$  species from the input hydrocarbon gas. Secondly, it is a necessary feature of the adsorption of carbon to the diamond lattice, as expanded upon in Section 1.3.4. A third key feature of atomic hydrogen is that it reacts favourably with graphitic carbon. As a result, the graphitic carbon can be etched from the film and hence this carbon is returned to the gas mixture, as discovered by Angus et al., as discussed in Section 1.2.2.<sup>8</sup> Additionally, atomic hydrogen has the ability to terminate any dangling bonds and thus in this way, the stability of the  $sp^3$  diamond lattice can be maintained. This prevents cross linkage and subsequent graphitization. Finally, it has the ability to break up any long chain hydrocarbons, thus inhibiting growth of any large structures on the diamond surface, the result of which would result in non-diamond growth. The role of atomic hydrogen in such a range of different aspects, from the gas phase chemistry to the growth process, emphasise its significance with respect to CVD diamond growth.<sup>1</sup>

### 1.3.2 Carbon Chemistry

In most cases, for MWPCVD diamond growth, a  $\text{CH}_4/\text{H}_2$  plasma is used with  $\text{CH}_4$  serving as the carbon precursor. However, there are a variety of alternatives that can be used in its place, provided one key condition is met. Initially, Eversole proposed that only those gases which could decompose to either methane or methyl radicals could be used as the hydrocarbon precursor.<sup>7</sup> However, in the early 90's, Bachmann et al.<sup>16</sup> discovered that diamond growth does not depend on the nature of the carbon precursor, provided that the C:H:O ratio of the gaseous mixture is appropriate, as illustrated in the Bachmann Triangle, Figure 1.5.

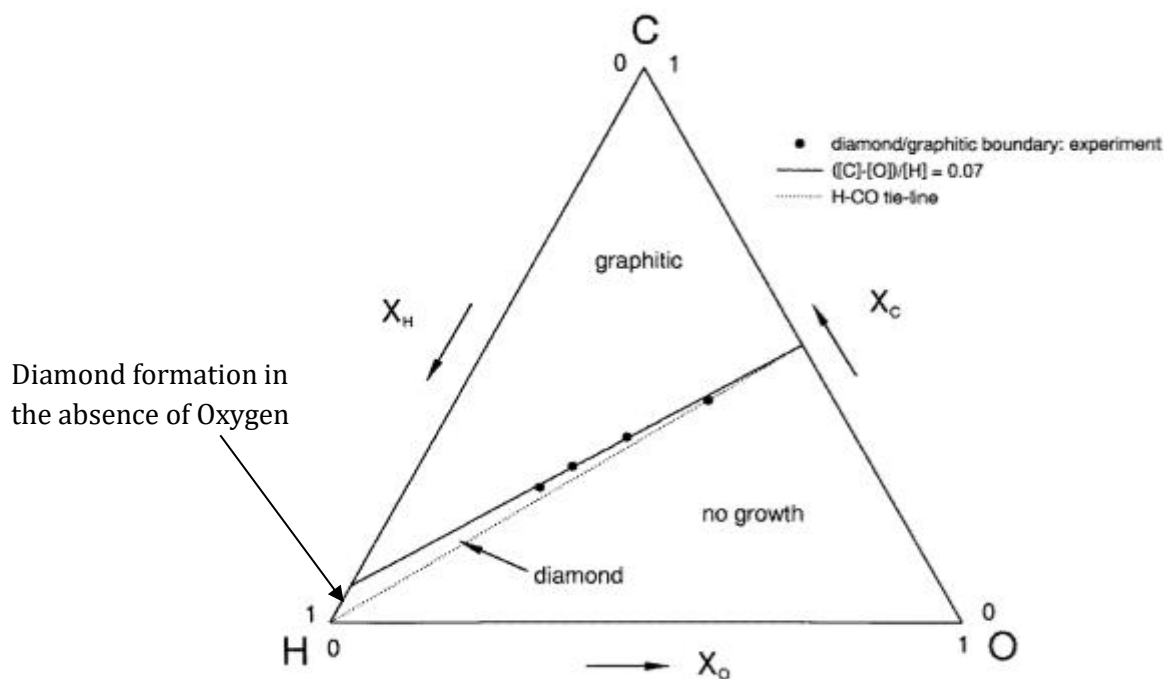
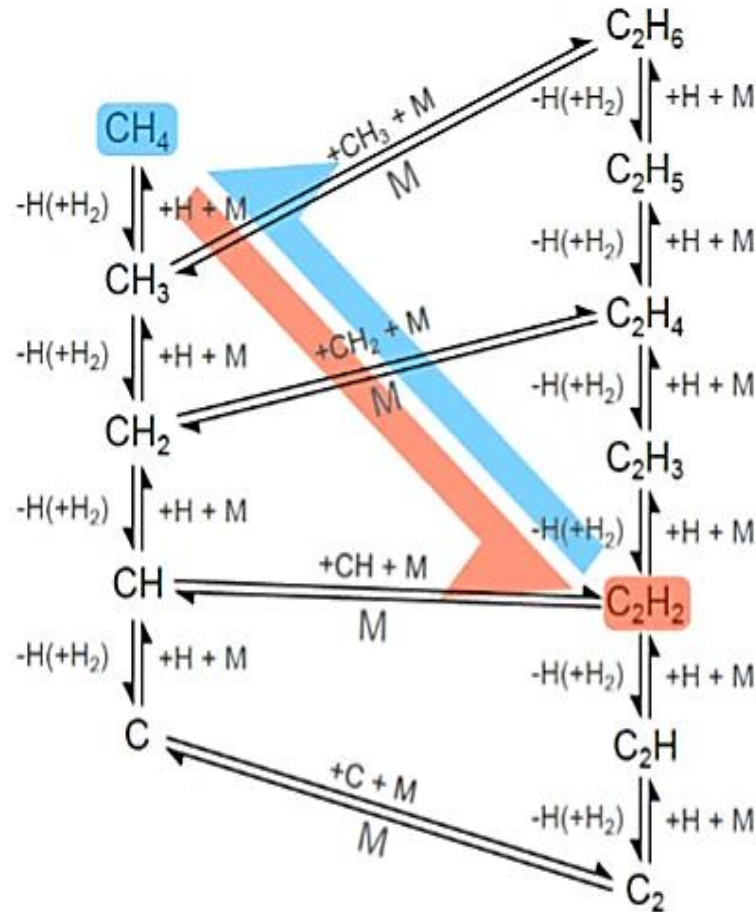


**Figure 1.4: Bachmann Triangle which illustrates the elemental C:H:O ratios needed for diamond growth to occur.<sup>17</sup>**

Each axis corresponds to the elemental ratio between two elements. For example,  $X_H = \frac{[H]}{([H] + [O])}$ , whereby  $[H]$  corresponds to the elemental concentration of H.

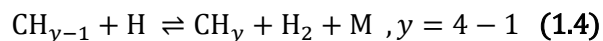
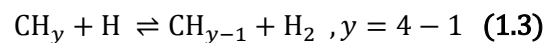
Therefore, with respect to a  $\text{CH}_4/\text{H}_2$  plasma, in the absence of oxygen, the system must contain hydrogen in large excess to carbon, as indicated in Figure 1.4. Additionally, the use of  $\text{CH}_4$  as opposed to longer hydrocarbons, such as  $\text{C}_2\text{H}_6$ , has been found to have no effect on the gas phase chemistry. This is due to the rapidity of the gas phase chemistry and so these longer hydrocarbons are effectively broken down into smaller components. Therefore, it is the ratio of elements C,H and O which determines the gas phase chemistry in the reactor and by extension, the growth and purity of the diamond film.

There are two main types of reaction that the hydrocarbon species undergo in the reactor, both of which are summarised in Scheme 1.1.



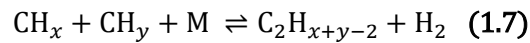
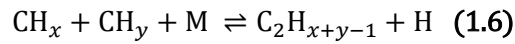
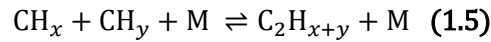
**Scheme 1.1: Summary of the gas phase carbon chemistry.**<sup>18</sup>

The first type involves hydrogen abstraction and addition reactions. Through reaction with atomic hydrogen, the hydrocarbon species either loses or gains a hydrogen, as shown in Reactions 1.3 and 1.4 respectively. <sup>15</sup>



As mentioned in Section 1.3.1, the driving force behind this type of reaction is the presence of atomic hydrogen, reiterating its importance in the MWPCVD process. However, these reactions are also dependent on  $T_{\text{gas}}$ . In the hotter regions of the reactor, H abstraction dominates, as shown in Reaction 1.3, resulting in the formation of  $\text{CH}_{y-1}$ , the most dominant species being  $\text{CH}_3$ . In the cooler regions, H addition dominates, Reaction 1.4.<sup>15</sup>

Radical recombination is the other predominant type of reaction that takes place in the reactor, as shown in Reactions 1.5 to 1.7, resulting in the formation of  $C_2H_z$  species. In a similar manner to  $CH_y$ , these species can undergo hydrogen abstraction and addition reactions, yielding species from  $C_2H_6$  to  $C_2$ . Of these  $C_2H_z$  species,  $C_2H_2$  is the most dominant form, as at high temperatures and in the presence of atomic hydrogen, species where  $z > 2$ , are rapidly converted to the more thermodynamically stable  $C_2H_2$ .<sup>15</sup>



For this type of reaction (radical recombination), the relationship that exists between  $CH_y$  and  $C_2H_z$  species, specifically between  $CH_4$  and  $C_2H_2$ , is key. The rate and direction of this conversion, as well as the number densities of these two species, is determined by  $T_{gas}$ . Therefore, it is important to consider how  $T_{gas}$  varies throughout the reactor, as discussed in Section 1.3.3.

### 1.3.3 Regions of the reactor

The key feature of all MWPCVD reactors is that they contain steep temperature gradients. For this reason, through modelling, the reactor can be viewed in terms of three regions of temperature, as evident in Figure 1.5.

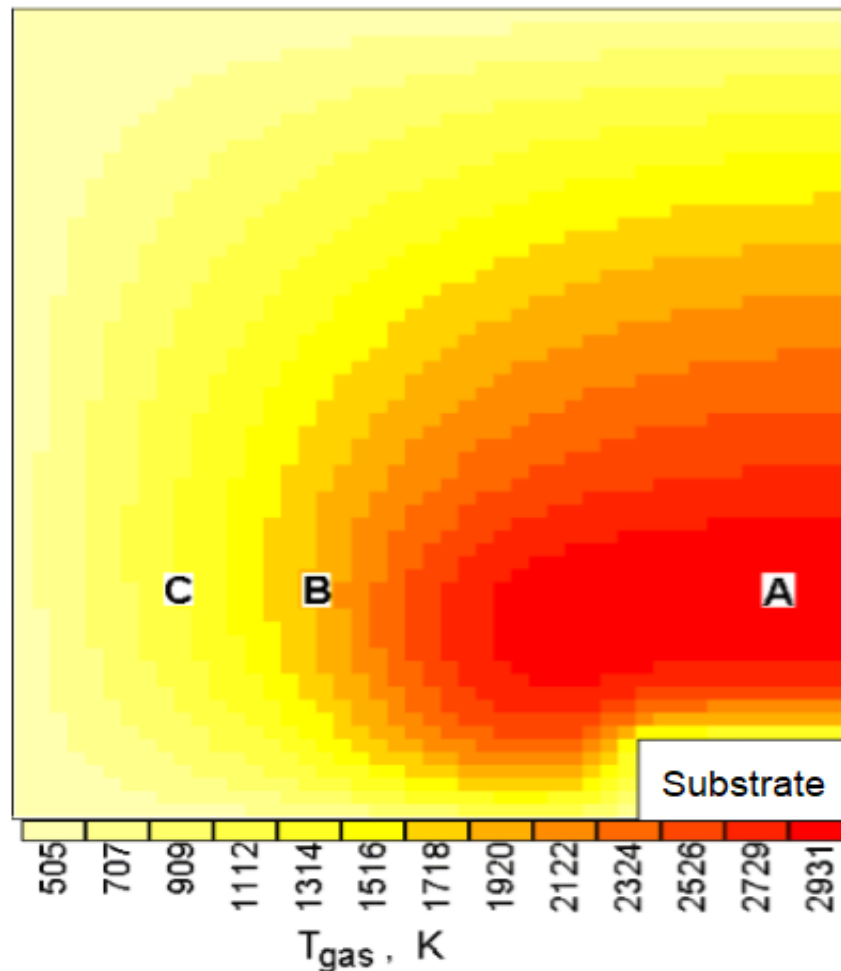


Figure 1.5: 2D ( $r, z$ ) plot of a modelled 4.4%  $\text{CH}_4/7\% \text{ Ar}/\text{H}_2$  plasma, illustrating the variation of  $T_{\text{gas}}$ , in Kelvin, with respect to position,  $r$ , within the reactor and height about the substrate,  $z$ .<sup>15</sup>

Figure 1.5 is a 2D theoretical model of a 4.4%  $\text{CH}_4/7\% \text{ Ar}/\text{H}_2$  mixture, under set base conditions defined by Butler et al.<sup>15</sup> showing the variation of  $T_{\text{gas}}$  throughout the reactor. These base conditions involved an applied microwave power,  $P = 1.5 \text{ kW}$  and total pressure,  $p = 150 \text{ Torr}$ . The diagram depicts a two-dimensional slice through a theoretical, cylindrically symmetric, three dimensional simulation of the 4.4%  $\text{CH}_4/7\% \text{ Ar}/\text{H}_2$  plasma. The y axis depicts the height above the substrate surface,  $z$ . This y axis spans across the entire height of the deposition chamber,  $h = 6 \text{ cm}$ . The x axis depicts the position within the reactor,  $r$ . It is worth noting that, with respect to the horizontal direction, Figure 1.5 only shows half of the slice that would be obtained from modelling. Therefore,  $r$  only spans across the radius of the deposition chamber,  $r_r = 6 \text{ cm}$ .<sup>12,15</sup>

At the core of the plasma, A,  $T_{\text{gas}}$  values tend to exceed 2200 K, whereas at higher r and z values, C,  $T_{\text{gas}}$  falls in the range  $500 < T_{\text{gas}} < 1400$  K. In region C, close to the water cooled walls of the chamber, at  $r = 6$  cm and  $z = 6$  cm,  $T_{\text{gas}}$  lies closer to 500 K than 1400 K. Therefore, movement to higher r and z values, as represented by A,B and C, corresponds to a decrease in  $T_{\text{gas}}$ . This feature makes the location of species within the reactor significant, in particular with respect to their concentrations.  $T_{\text{gas}}$  affects the number densities of species such as  $\text{CH}_4$  and  $\text{C}_2\text{H}_2$  in one of two ways. Firstly, in a system of this type, the total number density of a species has been found to be inversely proportional to  $T_{\text{gas}}$ . Secondly,  $T_{\text{gas}}$  is a determining factor with respect to the local number density of these species, due to its impact on the chemical kinetics.<sup>12,15</sup>

As stated in Section 1.3.2, the equilibrium between  $\text{CH}_4$  and  $\text{C}_2\text{H}_2$  is controlled by  $T_{\text{gas}}$ . The following explanation for this is aided by Figure 1.6. This shows the variation of the mole fractions of  $\text{C}_2\text{H}_2$  and  $\text{CH}_4$ ,  $X(\text{C}_2\text{H}_2)$  and  $X(\text{CH}_4)$  respectively, with respect to location in the reactor. The model shown in Figure 1.6 corresponds to a similar 4.4%  $\text{CH}_4$ /7%  $\text{Ar}/\text{H}_2$  plasma, under the same set of base conditions, with the only difference being that the height of the deposition chamber is defined as  $h = 6.2$  cm.<sup>12</sup>

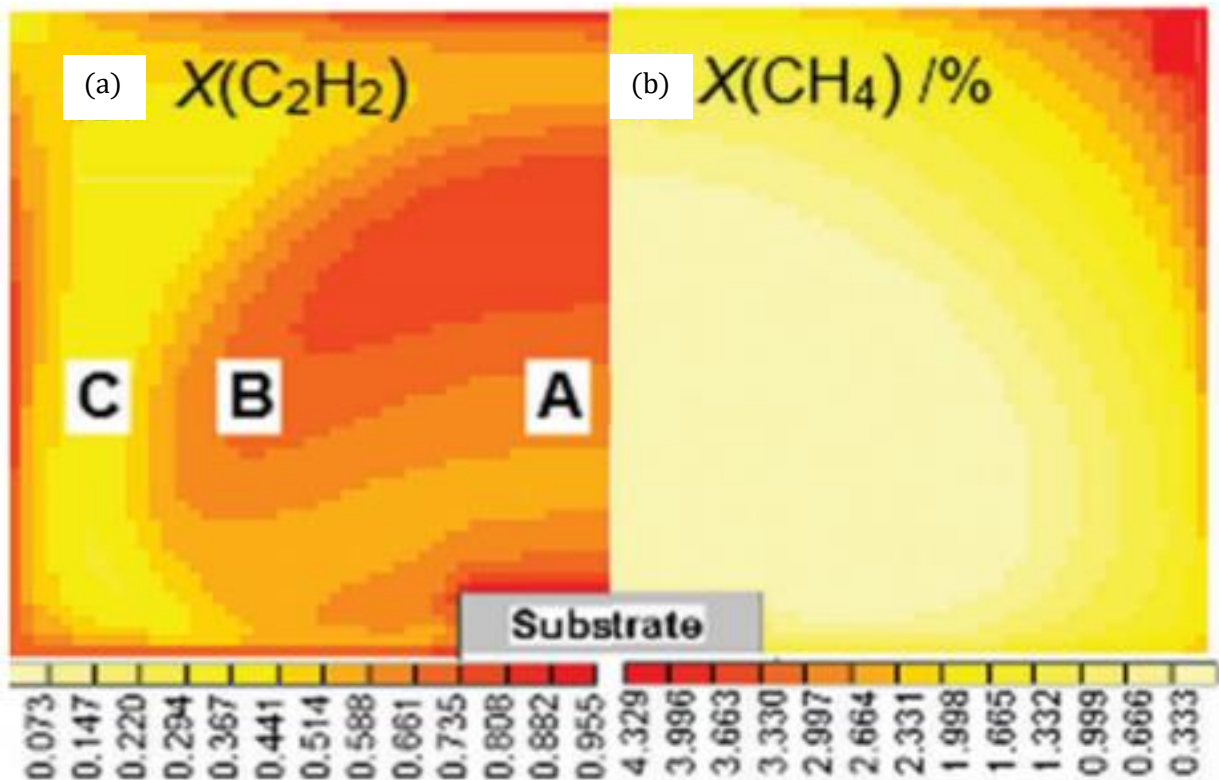


Figure 1.6: 2D ( $r,z$ ) plots of a modelled 4.4%  $\text{CH}_4$ /7% Ar/  $\text{H}_2$  plasma, illustrating the variation in the mole fractions of: (a)  $\text{C}_2\text{H}_2$ ,  $X(\text{C}_2\text{H}_2)$  and (b)  $\text{CH}_4$ ,  $X(\text{CH}_4)$ . Note that the values in (b) have been converted into % values, unlike those in (a).<sup>12</sup>

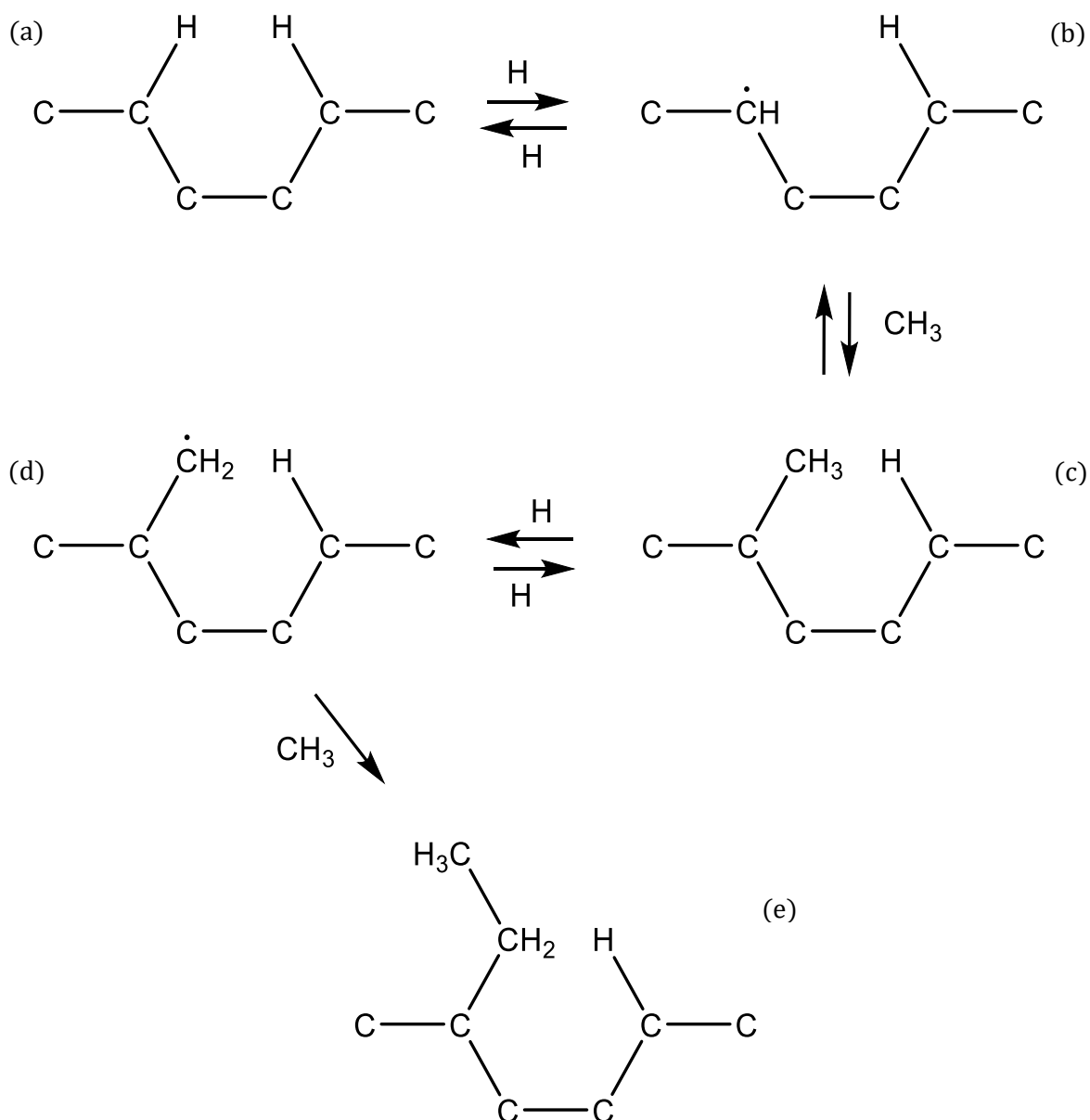
In the cooler region, C, the conversion lies in favour of  $\text{CH}_4$ . This can be determined since  $X(\text{C}_2\text{H}_2)$  is at its lowest, whilst  $X(\text{CH}_4)$  is simultaneously at its highest value. In contrast, at higher  $T_{\text{gas}}$ , as in region B, the relationship shifts in favour of the  $\text{C}_2\text{H}_2$  species. At the core of the plasma, A, it is evident that this conversion shifts further in favour of  $\text{C}_2\text{H}_2$ . In fact,  $\text{C}_2\text{H}_2$  has been found to account for more than 97% of the carbon content in this region.<sup>15</sup> Therefore, on movement from C to A, a greater proportion of  $\text{C}_2\text{H}_2$  is formed, as the rate of conversion of  $\text{CH}_4$  to  $\text{C}_2\text{H}_2$  increases with  $T_{\text{gas}}$ .

The above discussion highlights the impact of  $T_{\text{gas}}$  with respect to one specific equilibrium. However, as mentioned previously, the overall gas phase chemistry is much more complex. As shown in Scheme 1.1 for a  $\text{CH}_4/\text{H}_2$  mixture, in the presence of atomic hydrogen and high  $T_{\text{gas}}$ , multiple equilibrium relationships exist. Therefore, at any point in the reactor, all  $\text{CH}_y$  and  $\text{C}_2\text{H}_z$  species are present, in varying degrees. As  $T_{\text{gas}}$  is varied, this causes shifts in all of these equilibria and hence affects the local number densities of all of these species.

Having discussed several key aspects of the gas phase chemistry, Section 1.3.4 takes a look at the growth process and hence incorporation of carbon into the diamond lattice.

### 1.3.4 Addition of carbon unit to growing film

In considering the growth process, two aspects must be considered. The first step of the process involves an adsorption of a hydrocarbon species to the surface. Following this, the second step involves the incorporation of carbon, from this hydrocarbon species, into the lattice structure. A number of mechanisms have been put forward for the growth of the diamond film, specifically for this more complex second step. Scheme 1.2 shows a generic model for the pathway of the first step, as put forward in the paper by Butler and Woodin.<sup>19</sup>



**Scheme 1.2: Generic model for the adsorption of an ethyl species to the diamond surface**

As evident in (a), the surface is predominantly hydrogen terminated. Due to the abundance of atomic hydrogen in the gas mixture, a surface hydrogen can be abstracted, resulting in the formation of  $H_2$ , as well as a surface carbon radical as shown in (b). In such a system, the flux of atomic hydrogen is so high that in most cases, another hydrogen atom adsorbs into this vacant site, resulting in the formation of (a) and hence maintaining the hydrogen termination. However, for a small proportion of these radical sites, between 1 – 10%, a  $CH_3$  radical can collide and adsorb to the surface site, resulting in the formation of (c).<sup>15</sup> A second hydrogen abstraction, from the adsorbed  $CH_3$ , results in the formation of a radical site as in (d). To a small proportion of these sites, another  $CH_3$  radical can adsorb, forming (e).

In this way, an ethyl species has been added to the diamond surface, (e). Following this, there are a number of proposed reactions that such the species can undergo, as summarised by Butler and Woodin.<sup>19</sup> However, many combinations of these reactions were found to lead to the formation of a  $C_2H_4$  bridged species as presented in Figure 1.7. The species evidently shows that the carbon has been incorporated into the diamond lattice. It is important to note that the dominant pathway for the formation of the structure in Figure 1.7 is dependent on the gas phase chemistry.<sup>1,15,19</sup>

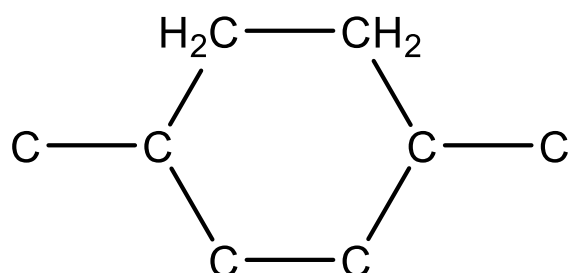


**Figure 1.7:  $C_2H_4$  bridged species**

With respect to both steps of the process, the gas phase chemistry is key in driving the growth of the diamond lattice. Therefore, an understanding of the gas phase chemistry is important with respect to the formation of CVD diamond. Under CVD diamond conditions, a range of different gases can be input, such as  $B_2H_6$  and  $N_2$ , resulting in Boron and Nitrogen doped diamond. The driving force behind this particular study is due to the interest surrounding silicon doped diamond.

## 1.4 Silicon Doped Diamond

### 1.4.1 Silicon-Vacancy Defect

A silicon vacancy centre arises from the replacement of two neighbouring carbon atoms by a silicon atom centred between the two vacancies. This Si atom sits in between the two sites in a split-vacancy configuration.<sup>20</sup> This is shown in Figure 1.8.<sup>21</sup> Following the initial discovery of these centres in CVD diamond only, these defects have also been identified in colourless, natural diamond, when treated with methods of Si incorporation.<sup>22</sup>

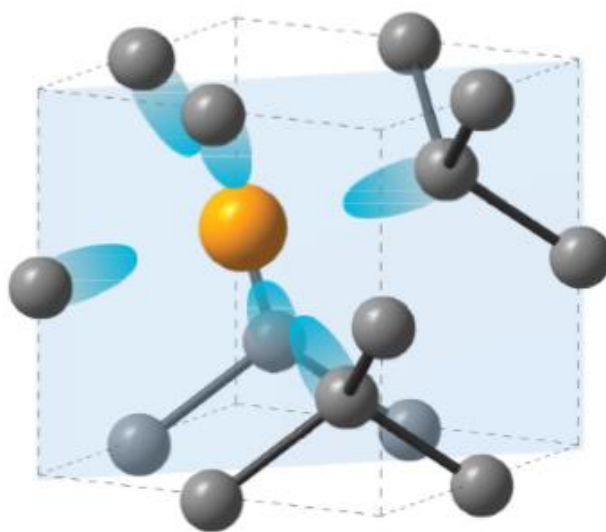


**Figure 1.8: Schematic of a Silicon-Vacancy centre in CVD diamond.** <sup>21</sup>

Silicon-vacancy centres can be observed in two different charge states. A neutral silicon-vacancy centre, denoted as SiV, has ten electrons associated with it, and a spin state of  $S = 1$ . Alternatively, negatively charged silicon-vacancy centres exist, denoted as SiV<sup>-</sup>. This complex contains an extra electron and hence has a spin state of  $S = 1/2$ .<sup>23</sup>

SiV<sup>-</sup> centres in diamond have been found to hold some unique properties. They have the ability to act as single photon sources, most of which are to a high degree indistinguishable; over 70% of these photons emit at a wavelength corresponding to a narrow zero phonon line, ZPL.<sup>20,24</sup> The ZPL is associated with photoluminescence from the centre, that has not been assisted vibronically. To highlight the significance of this property, the SiV<sup>-</sup> centre can be compared to negatively charged nitrogen vacancy centres, NV<sup>-</sup>. In a similar manner to its silicon counterpart, NV<sup>-</sup> centres form when two neighbouring carbon atoms are replaced by a nitrogen atom and a vacancy. These centres also act as single photon emitters. However, only 4% of photons emitted from NV<sup>-</sup> can be found in the ZPL.<sup>24</sup> In contrast, photons are emitted at a wider range of

wavelengths, as indicated by the wide ZPL of  $NV^-$ . Therefore, a much lower proportion of indistinguishable photons emit from the  $NV^-$  defect. This feature is also highlighted by the presence of much wider phonon sidebands associated with  $NV^-$  centres. Phonon sidebands correspond to the photons emitted with vibronic assistance. In contrast, for  $SiV^-$  centres, the sidebands are much weaker. Therefore,  $SiV^-$  centres have some optical properties, which might be considered superior to those of  $NV^-$  centres.<sup>24,25</sup>

The comparison between these two different centres is significant. The characteristic properties of  $NV^-$  have been greatly studied due to their promising applications with respect to quantum information processing, magnetometry, as well as in a biological aspect as fluorescent biomarkers.<sup>26,27,28</sup> However, the use of  $SiV^-$  centres is much more appealing with respect to these applications, particularly due to its superior optical properties. This is a key reason why the study of silicon doped diamond is necessary.

There are several other reasons driving research into silicon doped diamond. Although it can be viewed as a dopant, such as if the aim is to study the nature of these  $SiV^-$  centres, silicon in diamond can alternatively be viewed as an impurity. There are multiple methods of incorporating silicon into a  $CH_4/H_2$  plasma, as discussed in Section 1.4.2. However, it is important to note that regardless of whether the aim is to actively incorporate silicon or not, it is an inevitable impurity in a large proportion of CVD grown diamond. Most MWPCVD reactors, such as the one used in this particular study involves the use of a quartz window. Additionally, a large proportion of CVD growths are carried out on Si substrates. Both components are silicon sources, and so in the presence of a microwave activated plasma, silicon can be etched from their surfaces and incorporated into the gas phase chemistry. Therefore, an understanding of the silicon incorporation mechanism means that methods can be devised for reducing this impurity.

#### 1.4.2 Formation of silicon doped diamond

Several different methods have been put forward for the formation of silicon doped diamond.<sup>29</sup> In 2006, Wang et al. conducted a study into the formation of  $SiV^-$  centres by ion implantation.<sup>30</sup> This process involves the forced entry of Si ions into the CVD diamond film, through its surface.<sup>31</sup> Unlike ion implantation, the remaining three methods as discussed below, all form a part of the MWPCVD process. Silicon etching of the quartz window, the placement of a SiC plate underneath the substrate and the addition of silane to the input gas mixture all yield the same end product of Si doped diamond.<sup>32,33,34</sup>

Although Si doped diamond can be formed, there is still uncertainty regarding the mechanism by which these atoms are incorporated into the CVD diamond film. For this reason, studies involving

MWPCVD of diamond tend to be paired with spectroscopic techniques such as Optical Emission Spectroscopy, OES, which can reveal a lot about the system's gas phase chemistry, as discussed in Section 1.5.

## 1.5 Optical Emission Spectroscopy

Optical Emission Spectroscopy, OES, is a non-invasive technique used to detect certain emitting species of a system.<sup>35</sup> With respect to MWPCVD, it is used to detect excited state monoatomic and diatomic species, present in the plasma. On coupling OES with computational techniques, further information about these species can be obtained such as spatial distributions, which indicate how the relative emission intensities of these species vary as a function of their position, relative to the substrate surface.

OES has already been used in number of MWPCVD studies, such as in the investigation of a CH<sub>4</sub>/H<sub>2</sub>/Ar plasma. Ma et al.<sup>35</sup> investigated the behaviour of C<sub>2</sub>, CH and atomic H, as a function of total pressure and the input C/H ratio. This OES study was combined with computational programs to generate spatial distributions corresponding to each of these species. Different trends were observed with respect to each different species, an aspect which could be attributed to their different formation mechanisms. The presence of CH and C<sub>2</sub> from this study provides evidence for the proposed set of H abstraction and radical recombination type reactions that must be occurring, as discussed in Section 1.3.2.

OES is central to this study. Therefore, the operation of an Optical Emission spectrograph is discussed in Section 2.2, whilst Section 3.1 considers the data obtained.

## 1.6 Aims

The aim of this study is to investigate the variation of emissions from two Si-containing hydrogen plasmas, under varying process conditions, such as power, pressure and the ratio of the input gas mixtures. Silicon has been introduced into a hydrogen plasma through the use of (i) silane gas, SiH<sub>4</sub> and (ii) a Si substrate. From this data, a better understanding of the gas phase chemistry in a Si/H system can be achieved. It is important to understand a Si/H system first, as it should help in building the foundations needed to understand the more complex Si/ H/C system.

## 1.7 References

- 1) P. May, *Phil. Trans. R. Soc. Lond. A*, 2000, **358**, 473-495
- 2) E. H. L. Falcao and F. Wudl, *J. Chem. Technol. Biotechnol.*, 2007, **82**, 524-531
- 3) J. J. Gracio, Q. H. Fan and J. C. Madaleno, *J. Phys. D. Appl. Phys.*, 2010, **43**, 374017
- 4) T. S. V. Satyanarayana and R. Rai, *J. Interdisciplinary Dentistry*, 2011, **1**, 93-100
- 5) J. M. Zazula, On Graphite Transformations at High Temperature and Pressure Induced by Absorption of the LHC Beam, CERN LHC Project Note 78, 1997.
- 6) H.M Strong, *Am. J. Phys.*, 1989, **57**, 794-802
- 7) W. G. Eversole, 154 838, 1961. Us Pat., 3 030 188, 1961
- 8) J. C. Angus, H. A. Will and W. S. Stanko, *J. Appl. Phys.*, 1968, **39**, 2915-2922.
- 9) B. V. Spitsyn, L. L. Bouilov and B. V. Derjaguin, *J. Cryst. Growth*, 1981, **52**, 219-226.
- 10) S. Matsumoto, Y. Sato, M. Tsutsumi and N. Setaka, *J. Mater. Sci.*, 1982, **17**, 3106-3112.
- 11) M. Kamo, Y. Sato, S. Matsumoto and N. Setaka, *J. Cryst. Growth*, 1983, **62**, 642-644.
- 12) M. N. R. Ashfold, E. J. D. Mahoney, S. Mushtaq, B. S. Truscott and Y. A. Mankelevich, *Chem. Commun.*, 2017, **53**, 10482-10495.
- 13) E. J. D. Mahoney, S. Mushtaq, M. N. R. Ashfold, and Yu. A. Mankelevich, 'Spatially Resolved Optical Emission and Modelling Studies of Microwave-Activated H<sub>2</sub> Plasmas Operating under Conditions Relevant for Diamond Chemical Vapor Deposition', awaiting submission to *J. Phys. Chem. A*
- 14) Y. A. Mankelevich, M. N. R. Ashfold and J. Ma, *J. Appl. Phys.*, 2008, **104**, 113304.
- 15) J. E. Butler, Y. A. Mankelevich, A. Cheesman, J. Ma and M. N. R. Ashfold, *J. Phys. Condens. Matter*, 2009, **21**, 364021.
- 16) P. Bachmann, D. Leers and D. Wiechert, *J. Phys. IV*, 1991, **2**, 907-913
- 17) I. J. Ford, *J. Phys. D. Appl. Phys.*, 1996, **29**, 2229-2234.
- 18) M. Billing, Masters Thesis, University of Bristol, 2012
- 19) J. E. Butler and R. L. Woodin, *Phil. Trans. R. Soc. Lond. A*, 1993, **342**, 209-224.

- 20) E. Neu, D. Steinmetz, J. Riedrich-Möller, S. Gsell, M. Fischer, M. Schreck and C. Becher, *New J. Phys.*, 2011m **13**, 025012.
- 21) D'Haenens-Johansson *et al.*, *Phys. Rev. B*, 2011, **84**, 245208
- 22) C. M. Breeding and W. Wang, *Diam. Relat. Mater.*, 2008, **17**, 1335-1344.
- 23) T. Muller, C. Hepp, B. Pingault, E. Neu, S. Gsell, M. Schreck, H. Sternschulte, D. Steinmuller-Nethl, C. Becher and M. Atature, *Nat. Commun.*, 2014, **5**, 3328
- 24) L. J. Rogers, K. D. Jahnke, M. W. Doherty, A. Dietrich, L. P. McGuinness, C. Muller, T. Teraji, H. Sumiya, J. Isoya, N. B. Manson and F. Jelezko, *Phys. Rev. B*, 2014, **89**, 235101
- 25) I. Aharonovich, *Nat. Photonics*, 2014, **8**, 818-819.
- 26) M. W. Doherty, N. B. Manson, P. Delaney and L. C. L. Hollenberg, *New J. Phys.*, 2011, **13**, 025019.
- 27) L. Rondin, J. P. Tetienne, T. Hingant, J. F. Roch, P. Malentinsky and V. Jacques, *Rep. Prog. Phys.*, **77**, 056503.
- 28) G. Balasubramanian, A. Lazariev, S. R. Arumugam and D. wen Duan, *Curr. Opin. Chem. Biol.*, 2014, **20**, 69-77.
- 29) M. Prieske and F. Vollersten, *Diam. Relat. Mater.*, 2016, **65**, 47-52.
- 30) C. Wang, C. Kurtsiefer, H. Weinfurter and B. Burchard, *J. Phys. B At. Mol. Opt. Phys.*, 2006, **39**, 37-41.
- 31) D. P. Hickey, PhD thesis, University of Florida, 2007.
- 32) L. Rogers, K. D. Jahnke, M. H. Metsch, A. Sipahigil, J. M. Binder, T. Teraji, H. Sumiya, J. Isoya, M. D. Lukin, P. Hemmer and F. Jelezko, *Phys. Rev. Lett.*, 2014, **113**, 263602.
- 33) T. Teraji, T. Yamamoto, K. Watanabe, Y. Koide, J. Isoya, S. Onoda, T. Ohshima, L. J. Rogers, F. Jelezko, P. Neumann, J. Wrachtrup and S. Koizumi, *Phys. Status Solidi Appl. Mater. Sci.*, 2015, **212**, 2365-2384.
- 34) V. Sedov, V. Ralchenko, A. A. Khomich, I. Vlasov, A. Vul, S. Savin, A. Goryachev and V. Konov, *Diam. Relat. Mater.*, 2015, **56**, 23-28.
- 35) J. Ma, M. N. R. Ashfold and Y. A. Mankelevich, *J. Appl. Phys.*, 2009, **105**, 043302.

## 2. Experimental

### 2.1 Microwave Plasma CVD reactor

#### 2.1.1 MWPCVD reactor

For this study, a custom designed ASTEX type MWPCVD reactor was used, as shown in Figure 2.1. Figure 2.1 is split into two images, with the right side showing the reactor itself, whilst the left hand side illustrates the reactor's components.

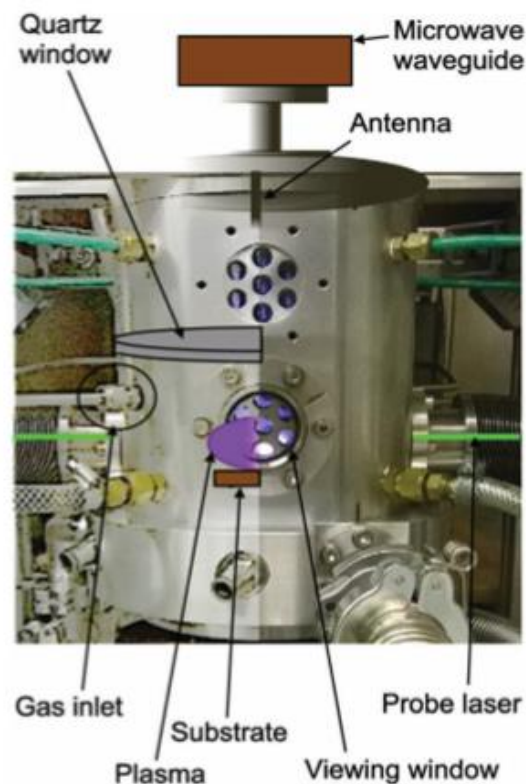


**Figure 2.17: The custom designed ASTEX type MWPCVD reactor used. The left half schematically shows the reactor's components. <sup>1</sup>**

The microwaves are generated by a 2 kW, 2.45 GHz Muegee power supply and generator, as shown in Figure 2.2 (a).<sup>2</sup> These are passed through a waveguide and tuned through three tuning forks, converting them from the  $TE_{10}$  mode to the  $TM_{01}$  mode. The microwaves are then fed into the reactor through an antenna, into a water cooled, vertical metal cylinder with a volume of  $\sim 600 \text{ cm}^3$ .<sup>3</sup> The chamber is divided into two regions by a quartz window with a vacuum seal. The bottom component, the deposition chamber, is evacuated to a base pressure of  $\sim 0.018 \text{ Torr}$ .

The feed gases flow from the gas cylinders shown in Figure 2.2 (c), through gas feed lines, into the chamber. The flow of each gas is controlled and monitored by calibrated mass flow controllers, measuring flow in units of sccm, standard cubic centimetre per minute. On reaching the reactor, the gases, having been mixed together, are fed in through eight cylindrically symmetric gas inlets. These gas inlets are located below the quartz window as indicated in Figure 2.1. Therefore, as the microwaves passed through the quartz window, they interacted with the gas mixture, resulting in a microwave activated plasma, as discussed in Section 1.3.1. It is important to note that for the two systems studied, the microwave activated plasma was initially created in a pure  $H_2$  system. On reaching base conditions,  $SiH_4$  and Ar were then flown into the reactor, as discussed in Sections 2.1.2 and 2.1.3 respectively.

(a)



(b)



(c)



**Figure 2.2: Images of the (a) 2 kW, 2.45 GHz Muegge power supply and generator, (b) Gas cylinders of the feed gases and (c) Central system which controlled the individual mass flow controllers**

Both gas mixtures studied were conducted in the presence of a molybdenum substrate of diameter,  $\phi_{\text{sub}} = 32$  mm. The substrate was sat on coiled Mo wire spacer,  $\phi_{\text{wire}} = 32$  mm. Both were placed centrally on the base plate. Although the same substrate was used in both cases, the thickness of the spacer wire differed. The thickness of the wire is important with respect to controlling the temperature of the substrate,  $T_{\text{sub}}$ . The thinner the wire, the smaller the distance between the substrate and the water cooled base plate. Therefore, a thinner wire results in a lower  $T_{\text{sub}}$ , as discussed further in Section 2.1.3.

### 2.1.2 SiH<sub>4</sub>/H<sub>2</sub> plasma

As mentioned in Section 1.6, two different microwave-activated silicon-containing hydrogen plasmas were generated and observed in this study.

The first involved a 0.1% SiH<sub>4</sub> in H<sub>2</sub> mixture, henceforth SiH<sub>4</sub>/H<sub>2</sub> plasma. This system was studied as a function of: flow rate of 0.1% SiH<sub>4</sub> in H<sub>2</sub> mixture,  $F(\text{SiH}_4)$ , applied forward microwave power,  $P$  and total pressure,  $p$ .

Therefore, a set of base values for all parameters had to be established. Throughout all studies, H<sub>2</sub> flow rate,  $F(\text{H}_2)$  remained constant at 300 sccm.  $P$  and  $p$  were set as 1.5 kW and 150 Torr respectively, values which have been determined through previous studies conducted.<sup>4</sup> For the first part of the experiment,  $F(\text{SiH}_4)$  was varied from 0 – 44 sccm. From the data collected, a base value of 15 sccm was established, reasons for which are discussed in Section 3.3.2. After the base value for  $F(\text{SiH}_4)$  had been determined,  $P$  was varied from 0.7 to 1.85 kW. Finally,  $p$  was varied from 50 to 275 Torr.

An additional point to add is that a 0.01" thick Mo wire spacer was used in this study.

### 2.1.3 Si substrate present in H<sub>2</sub>/Ar

The second system studied, examined emissions from a hydrogen, with a 0.7 mm thick Si wafer present, sitting on the Mo substrate. A thinner spacer wire of 0.002" was used to yield a  $T_{\text{sub}} < 600$  °C at base conditions of  $F(\text{H}_2) = 300$  sccm,  $F(\text{Ar}) = 0$  sccm,  $P = 1.5$  kW and  $p = 150$  Torr.

This particular silicon-containing hydrogen plasma was studied as a function of argon flow rate,  $F(\text{Ar})$ . The flow rate of H<sub>2</sub> was kept constant at 300 sccm, whilst Ar was added at three different flow rates: a pure H<sub>2</sub> plasma (0% Ar), a 3:1 mixture of H<sub>2</sub> (equivalent to 25% Ar, achieved by introducing 100 sccm Ar) and a 1:1 mixture (50%). The pumping rate was adjusted to ensure total  $p$  was maintained at 150 Torr.

Two repeats of the study were conducted, both of which used the same Si wafer. However, following the first repeat, the Si wafer had evidently been affected on exposure to the H<sub>2</sub>/Ar plasma. Therefore, the first repeat was carried out with a relatively smooth, clean Si wafer. Meanwhile, the second repeat was carried out with the same, now rougher Si wafer.

Each repeat was made up of two runs.  $F(\text{Ar})$  was initially increased from 0 to 300 sccm, with OES spectra recorded at the three flow rates of interest. Following this,  $F(\text{Ar})$  was brought back down to 0 sccm and left for a period of ten minutes.  $F(\text{Ar})$  was then increased for a second time, with another set of OES spectra recorded.

## 2.2 Optical Emission Spectrometry

The Optical Emission Spectrometer used was composed of two parts: a Czerny-Turner spectrograph (Andor Shamrock 500i) and a Charge Coupled Device detector, a CCD detector (Andor Newton 970).<sup>5</sup>

### 2.2.1 Andor Shamrock 500i Spectrograph

This piece of equipment is very similar in design to a Czerny-Turner monochromator. The only difference being that an exit slit is not present. Instead, it has been replaced by a CCD detector, making it a spectrometer.

As shown in Figure 2.3, the role of a monochromator is to divide up incoming light, A, according to wavelength, with each wavelength being focused to a different position on F, the exit slit. With respect to the spectrometer used, since the exit slit was not present, a camera was placed at the focus distance enabling a wavelength range to be detected simultaneously.

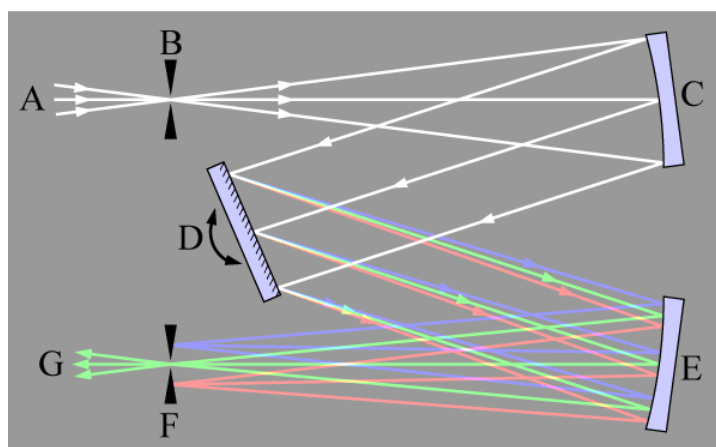


**Figure 2.38: Schematic diagram of the Czerny-Turner monochromator<sup>5</sup>**

Emissions from the full height of the plasma, A, pass through the entrance slit, B, into the spectrometer. On hitting the collimating mirror, C, these rays of light are collimated, resulting in a parallel alignment. These are then diffracted by the grating, D. In this case, D is a grating turret with direct digital drive. As a result, the rays of light are separated by wavelength. Reflection by a focusing mirror, E, means that each wavelength is focused to a different position. In this present study, all of these wavelengths were passed to the CCD detector.

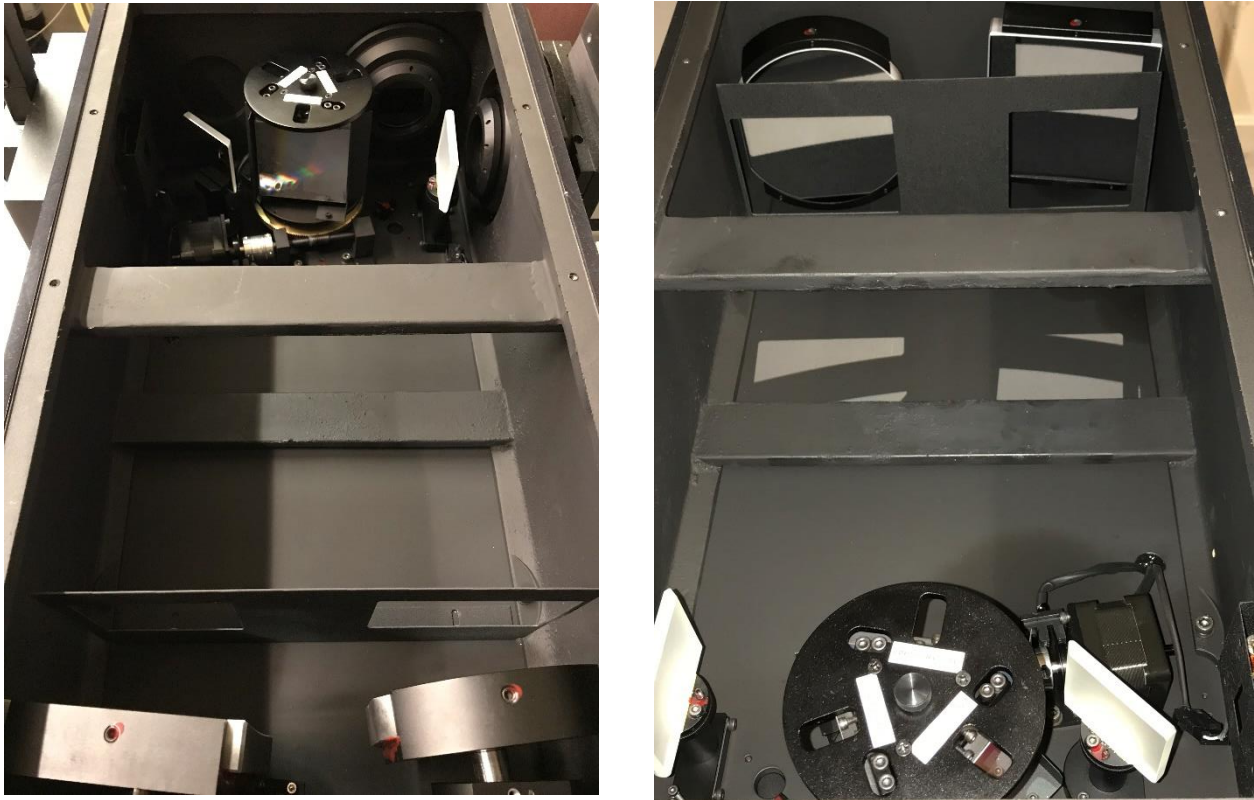


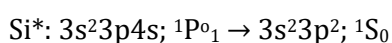
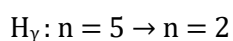
**Figure 2.4: Top down view of the Andor Shamrock 500i Spectrograph**

### 2.2.2 Andor Newton 970 CCD detector

This light was imaged using a cooled CCD detector. The role of the CCD detector is to image the emissions and their relative intensities, as a function of wavelength. It was important that the detector was cooled to  $-60^{\circ}\text{C}$ , in order to reduce background noise and hence increasing the signal to noise ratio. The CCD is a 2D array of pixels, and hence in this way it is divided up into smaller areas. As a photon falls on one of these smaller areas, it is absorbed and results in the release of one or more electrons, inferring an intensity.<sup>6</sup> Therefore, the intensity of an emission is proportional to the number of electrons released at each pixel. It was through this process that OES spectra, such as Figure 3.1, were constructed which showed the emissions generated from the plasma, as a function of wavelength.

### 2.2.3 Specific Emissions Observed

As stated in Section 1.5, OES was used to observe emissions of small species, in particular Si containing species, present in the two gas mixtures. The wavelength region 375 – 445 nm was focused on, since it contained three key emissions, corresponding to H $\gamma$  at ~ 434 nm, Si\* at ~ 390 nm and a SiH\* band centred around ~ 414 nm.<sup>7,8</sup> The \* symbol now signifies that the species is a ro-vibronically excited state species. The specific transitions are shown in Scheme 2.1.



**Scheme 2.1: The exact transitions corresponding to the emissions observed by OES at 390, 414 and 434 nm. <sup>7,8</sup>**

These emissions were important as they provided evidence for the presence of excited atomic H, Si and SiH species in the gas mixture. Therefore, the three emissions listed in Scheme 2.1 were observed in both microwave activated gas mixtures, as a function of the parameters laid out in Sections 2.1.2 and 2.1.3 respectively.

## 2.3 Computational Programs

Having obtained OES spectra for each set of conditions, the computational programs of MATLAB and PGOPHER were necessary in determining relative emission intensity values for each of the species, as a function of height above the Mo substrate surface. These data was then plotted using ORIGIN, generating a series of spatial distributions, discussed in Section 3.

With respect to the monoatomic species of  $H^*$  and  $Si^*$ , MATLAB alone was sufficient to determine these values and hence generate these profiles. However, for the  $SiH^*$  emissions, PGOPHER was also needed. PGOPHER is a software which has the ability to simulate spectra for molecular species.<sup>9, 10</sup> Therefore, through the input of vibrational constants corresponding to  $SiH(A-X)$ , obtained from Herzberg et al.<sup>11</sup>, a simulation for the  $SiH^*$  band was generated, as illustrated by the black spectrum in Figure 2.5. Following the generation of a simulated spectrum, PGOPHER can be used to conduct a fitting process, whereby experimentally obtained spectrum can be fitted to this simulation. This process is explained in depth in Section 3.2. However, the key point to draw is that this process generated relative emissions intensity values for  $SiH^*$  at different heights above the substrate.

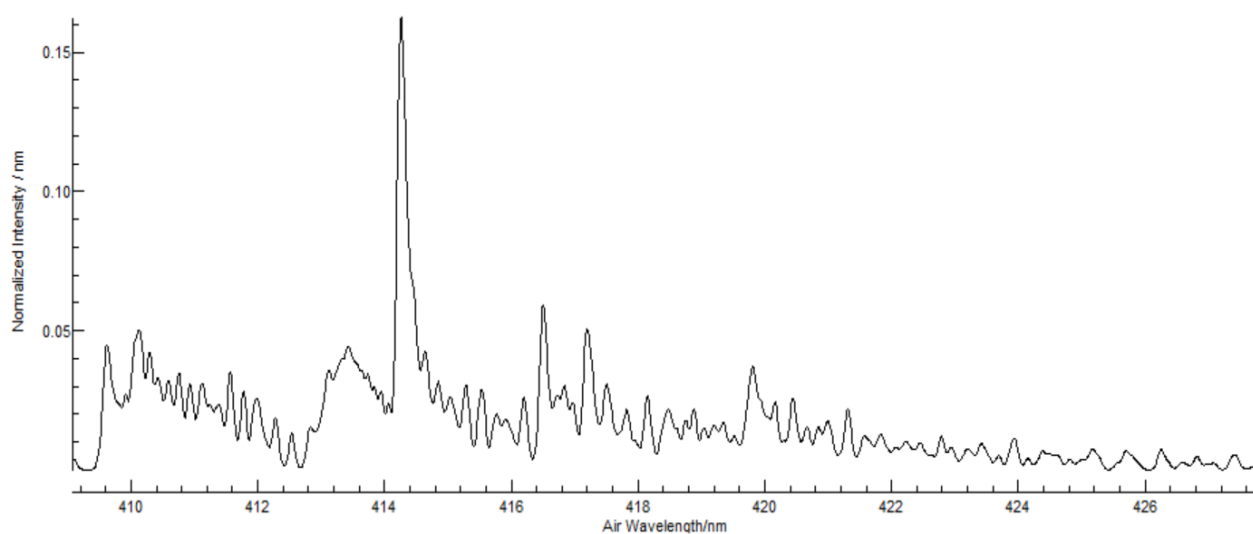


**Figure 2.5: Simulated spectrum for  $SiH(A-X)$ , generated by PGOPHER.**

## 2.4 Scanning Electron Microscopy, SEM

Scanning Electron Microscopy, SEM is an analytical technique used to determine several properties about the surface of a sample, such as its elemental composition and its topography. The process involves firing a beam of electrons at the sample's surface. The electrons interact with the atoms on the surface, and as a result, a variety of different components are emitted in response. These include secondary electrons, backscattered electrons and X-rays. These different components feed into their respective detectors, attached to the SEM. In this way, information about the sample's surface can be determined.<sup>12</sup>

In the study presented here, a JEOL IT300 SEM, as shown in Figure 2.6 was used to examine the surface roughness of the two Si substrates used in the H<sub>2</sub>/Ar study, as discussed in Section 2.1.3.



**Figure 2.6: An image of the JEOL IT300 Scanning Electron Microscope used in this study.<sup>13</sup>**

The two Si substrates examined by SEM are shown in Figure 2.7. Figure 2.7 (a) shows the substrate having been exposed to the H<sub>2</sub>/Ar plasma, whilst (b) is the clean, unexposed Si substrate.

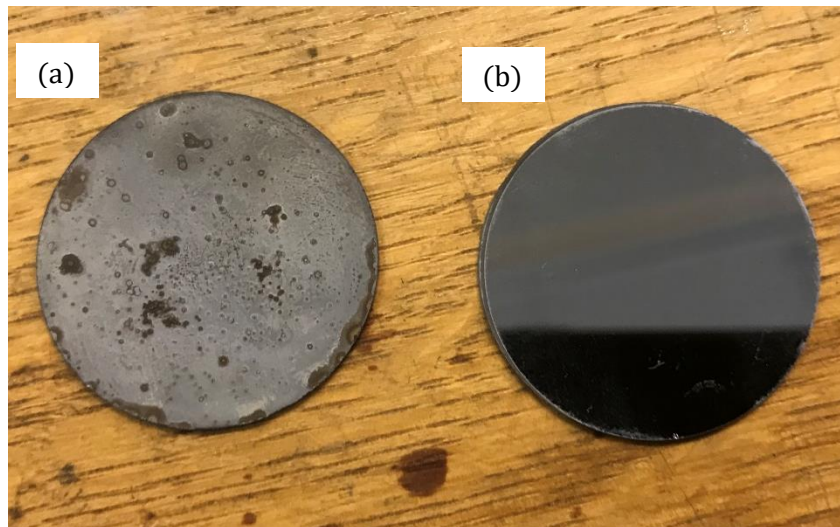


**Figure 2.7: The two Si substrates imaged by SEM: (a) Si wafer exposed to the H<sub>2</sub>/Ar plasma and (b) Clean, unexposed Si wafer**

The samples were broken into smaller pieces, such that they could be stuck onto 12 mm thick SEM stubs, through the use of carbon sticky pads. Before SEM imaging could take place, the surfaces of these samples were coated with 15.9 nm of silver, in an Agar High Resolution Sputter Coater. In order for SEM imaging to occur, the sample surface must be conductive. It is for this reason that the samples were coated with Ag. The samples were then placed in the JEOL IT300, with the accelerating voltage of the electron beam set to 15.0 kV. Images relating to the secondary electrons and backscattered electrons, SED and BED images respectively, were collected at a range of different magnifications, at a working distance ~ 10 mm.

It is important to note that the use of SEM was not central to this study. However, it was an additional technique which aided in the analysis of the H<sub>2</sub>/Ar system with a Si substrate present. Its use yielded some interesting observations, as discussed in Section 3.4.3, hence its inclusion in this study.

## 2.5 References

- 1) M. N. R. Ashfold, E. J. D. Mahoney, S. Mushtaq, B. S. Truscott and Y. A. Mankelevich, *Chem. Commun.*, 2017, **53**, 10482-10495.
- 2) J. Ma, M. N. R. Ashfold and Y. A. Mankelevich, *J. Appl. Phys.*, 2009, **105**, 043302.
- 3) A. Cheesman, J. A. Smith, M. N. R. Ashfold, N. Langford, S. Wright and G. Duxbury, *J. Phys. Chem. A*, 2006, **110**, 2821-2828.
- 4) E. J. D. Mahoney, B. S. Truscott, M. N. R. Ashfold and Y. A. Mankelevich, *J. Phys. Chem. A*, 2017, **121**, 2760-2772.
- 5) Allen Group at Ohio State University, <https://research.cbc.osu.edu/allen.697/wp-content/uploads/2012/05/Resolution-presentation1.ppt>, (accessed April 2018).
- 6) UCL Mullard Space Science Laboratory, [http://www.mssl.ucl.ac.uk/www\\_detector/ccdgroup/opttheory/ccdoperation.html#basics](http://www.mssl.ucl.ac.uk/www_detector/ccdgroup/opttheory/ccdoperation.html#basics), (accessed April 2018)
- 7) W. C. Martin and R. Zalubas, *J. Phys. Chem. Ref. Data*, 1983, **12**, 323-380.
- 8) K. P. Huber and G. Herzberg, "Constants of Diatomic Molecules" (data prepared by J. W. Gallagher and R. D. Johnson, III) in **NIST Chemistry WebBook, NIST Standard Reference Database Number 69**, Eds. P. J. Linstrom and W. G. Mallard, National Institute of Standards and Technology, Gaithersburg, MD, 20899, doi: 10.18434/T4D303, (accessed April 2018).
- 9) C. M. Western, *J. Quant. Spectrosc. Radiat. Transfer*, 2017, **186**, 221-242.
- 10) PGOPHER, A Program for Simulating Rotational, Vibrational and Electronic Spectra, C. M. Western, University of Bristol, <http://pgopher.chm.bris.ac.uk>
- 11) G. Herzberg, A. Lagerqvist and B. J. McKenzie, *Can. J. Phys.*, 1969, **47**, 1889-1897.
- 12) K. D. Vernon-Parry, *III-Vs Review*, 2000, **13**, 40-44.
- 13) UoB School of Chemistry, <http://www.bristol.ac.uk/chemistry/facilities/electron-and-scanning-probe-microscopy/>, (accessed April 2018)

## 3. Results and Discussion

### 3.1 OES spectrum

Figure 3.1 shows an example of the type of OES spectrum generated, with the x axis corresponding to wavelength in nm and the y axis representing height in pixels. As explained in Section 2.2.3, the wavelength region 375 – 445 nm was observed in particular, as it meant that emissions corresponding to H\*, Si\* and SiH\* were visible, as highlighted in Figure 3.1.

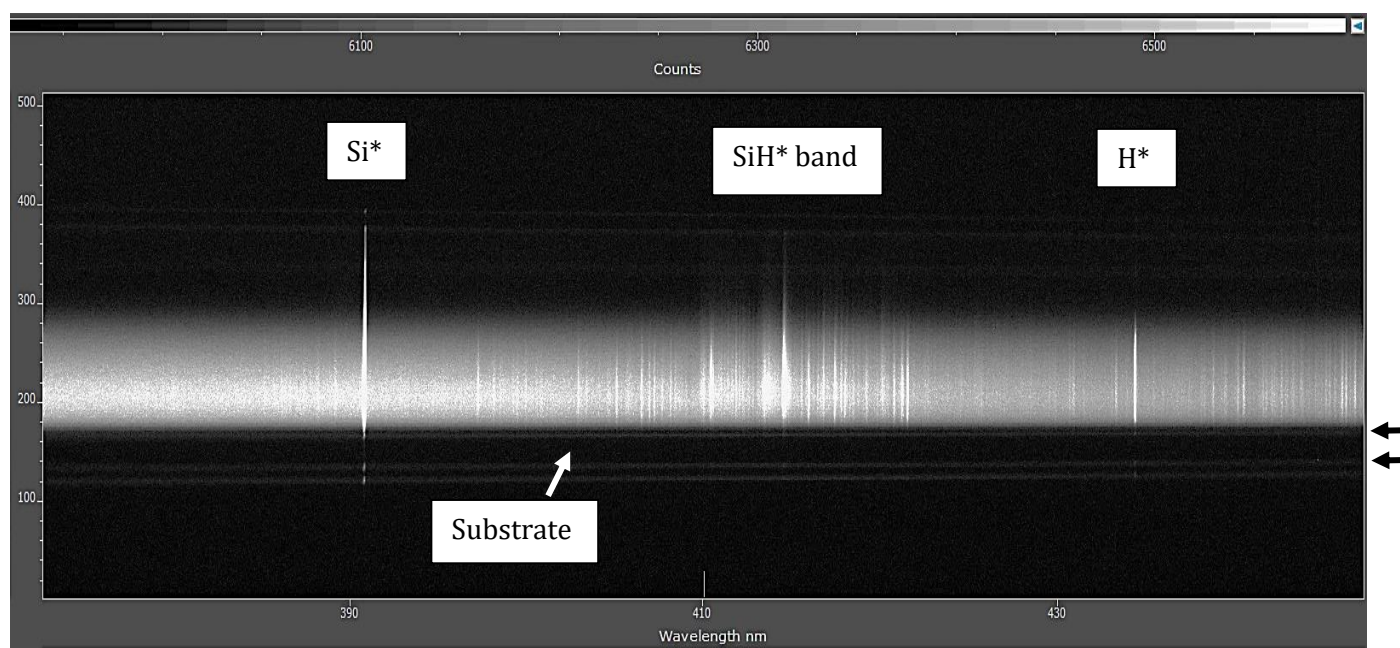


**Figure 3.19: Example of OES spectrum collected. This particular spectrum corresponds to SiH<sub>4</sub>/H<sub>2</sub> plasma, at  $P = 0.9$  kW, with all other parameters at 'base conditions'**

However, although this type of spectrum showed the emissions of interest, there were clearly other features present. Directly below the visible emissions, two horizontal lines were observed, as highlighted by the black arrows in Figure 3.1. These indicated the presence of the Mo substrate. The higher of the two lines corresponded to top of the substrate, henceforth referred to as the substrate surface,  $z$ .

Due to the exceeding number of emission lines, relative to the three emissions of interest, the OES spectra clearly showed the presence of other excited species in the system. Although it is difficult to identify the transition corresponding to each emission line, it is believed that the majority of these lines originated from H<sub>2</sub>\*. For example, a H<sub>2</sub>\* ( $a^3\Sigma^+_g - b^3\Sigma^+_u$ ) transition has been reported to correspond to a continuum emission observed in the wavelength region of 200 to 450 nm. This type of emission most likely arises through electron impact excitation of H<sub>2</sub> to the triplet  $a^3\Sigma^+_g$

state, a bound state. This state can also be populated following radiative cascade from higher energy triplet states, since the  $a^3\Sigma_g^+$  state is relatively more stable. This  $a^3\Sigma_g^+$  state can then radiate to the free  $b^3\Sigma_u^+$  state. This particular continuum emission cannot be observed as discrete lines but as a glow instead. It has also been found to be more intense towards the lower wavelength of 200 nm.<sup>1</sup> From Figure 3.1, these features do seem present with a glow in the background, which appears more intense towards 375 nm as opposed to 445 nm, thus suggesting the presence of  $H_2^*$ .

A second feature observed on Figure 3.1 was that there were regions of height in which no emissions could be seen, as indicated by the black regions at the top and bottom of the spectrum.

Figure 3.1 shows an example of the initial data collected. However, as stated in Section 2.3, the following step involved the computational processing of this data, with the overall aim of generating relative emission intensity values for the species in question and hence spatial profiles. The MATLAB program was fundamental to this process, as shown in Figure 3.2, a false colour plot. This plot is an alternative representation of the data shown in Figure 3.1. It contains the same information, with several key differences.

Firstly, as shown in Figure 3.1, a subtle skew is evident. One of MATLAB's main functions in this study was to correct for this skew, as evident in Figure 3.2. Secondly, the region of height has been narrowed, hence omitting the regions of height containing no emission. In this way, the height was also being considered relative to the substrate surface, in mm, instead of pixels. A final additional difference between the two figures was that only the emissions of interest were highlighted. This is because the false colour plot is a 3-D plot, with the z-axis corresponding to intensity. In this way, due to the relatively higher intensities of the three species in question relative to the other emissions present, only these three emissions were represented on Figure 3.2.

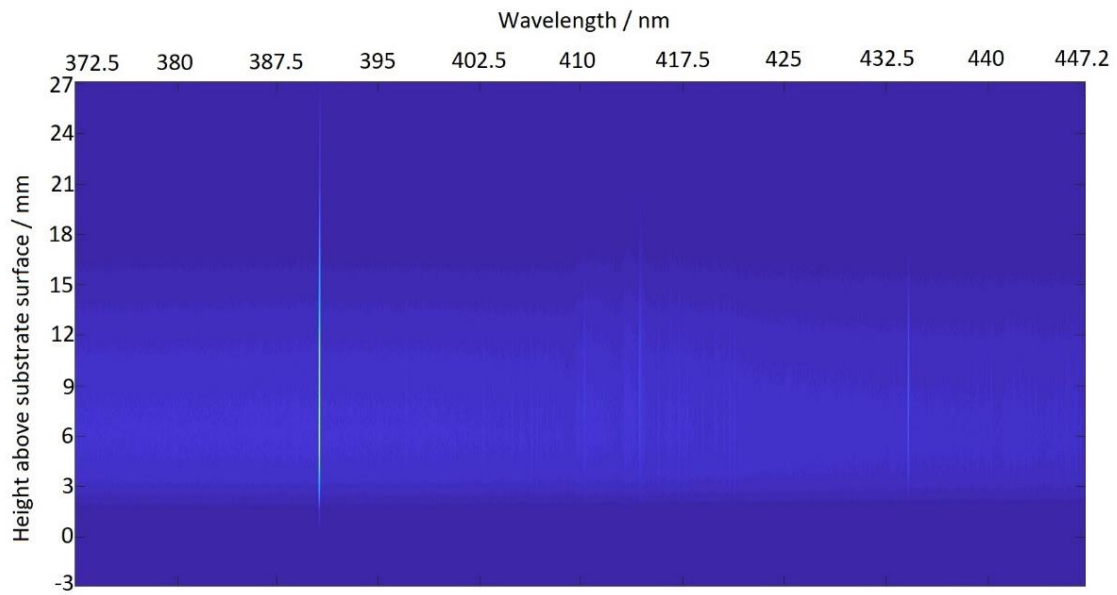


**Figure 3.2:** False colour plot indicating intensity as a function of wavelength (x-axis) and height (y-axis). The plot shown here corresponds to the  $\text{SiH}_4/\text{H}_2$  plasma, at  $P=0.9$  kW, with all other parameters at 'base conditions'.

With respect to the y axis, height above the substrate surface, the use of MATLAB has a second important function which aided analysis. It has the ability to divide the above plot into smaller regions, through a process referred to as 'binning'. In this way, the emissions can be observed and analysed at different heights. Therefore, relative emission intensity values for  $\text{H}^*$  and  $\text{Si}^*$  were determined as a function of height above the substrate. For  $\text{SiH}^*$ , the PGOPHER program had to also be used to determine these values, as discussed in Section 3.2.

## 3.2 PGOPHER Fit

In the case of SiH\*, the region of  $z = -3$  to 27 mm was divided into twenty smaller regions of 1.5 mm each. Each region was then fitted to the simulated spectrum for SiH (A-X) using PGOPHER. An example of the PGOPHER process is shown in Figures 3.3 and 3.4. Figure 3.3 shows the comparison between the experimental and simulated spectra before the fit was carried out. In this particular example, this data corresponds to 0.9 kW, at a height of  $z = 9.75 \pm 0.75$  mm. The top spectrum in red represents the experimental data, whilst the black spectrum on the bottom is the simulated spectrum generated by PGOPHER, as discussed in Section 2.3.<sup>2</sup>

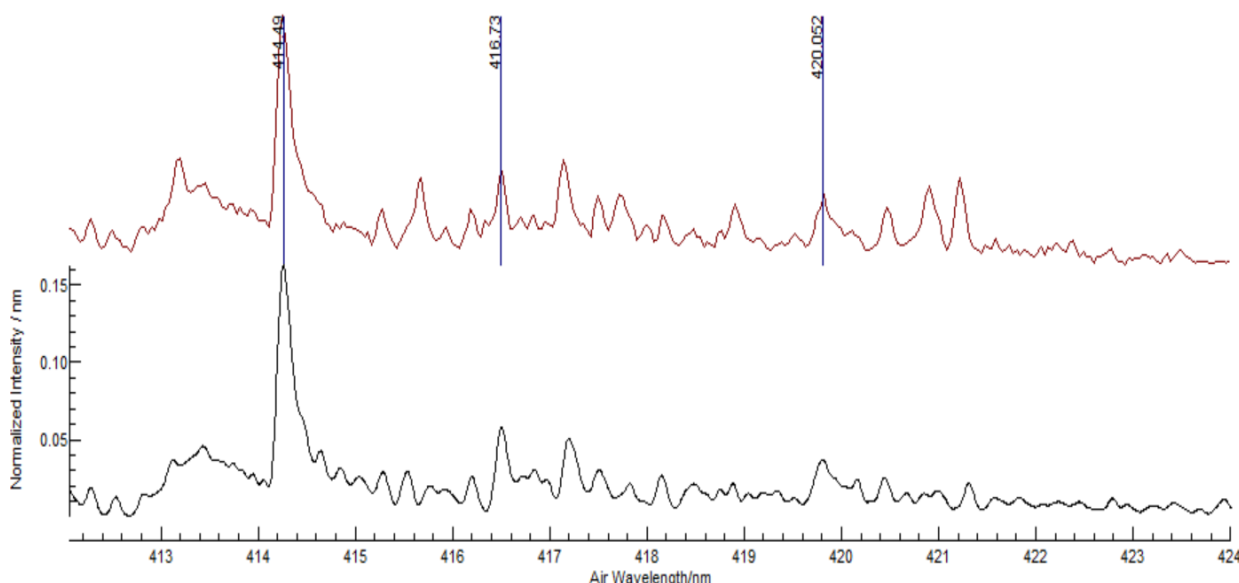


**Figure 3.3: PGOPHER Fitting process of SiH (A-X) in a SiH<sub>4</sub>/H<sub>2</sub> plasma, corresponding to  $P = 0.9$  kW,  $z = 9.75 \pm 0.75$  mm. The red spectrum corresponds to the experimentally obtained spectrum.<sup>2</sup>**

Figure 3.4 shows the fit of the experimental spectrum, from Figure 3.3, to the simulated spectrum. The fit itself is shown in Figure 3.4 (a), whilst Figure 3.4 (b) shows the difference between the two, including the presence of any residual peaks not corresponding to SiH\*. These residual peaks can be attributed to H\* and H<sub>2</sub>\* species, as they have been observed in a pure H<sub>2</sub> plasma, a study which had previously been conducted by the group.<sup>1</sup> Overall, from these fits, values for the relative emission intensity of SiH\* were determined, each corresponding to a different height. By compiling these values together, a spatial distribution for SiH\* was created.

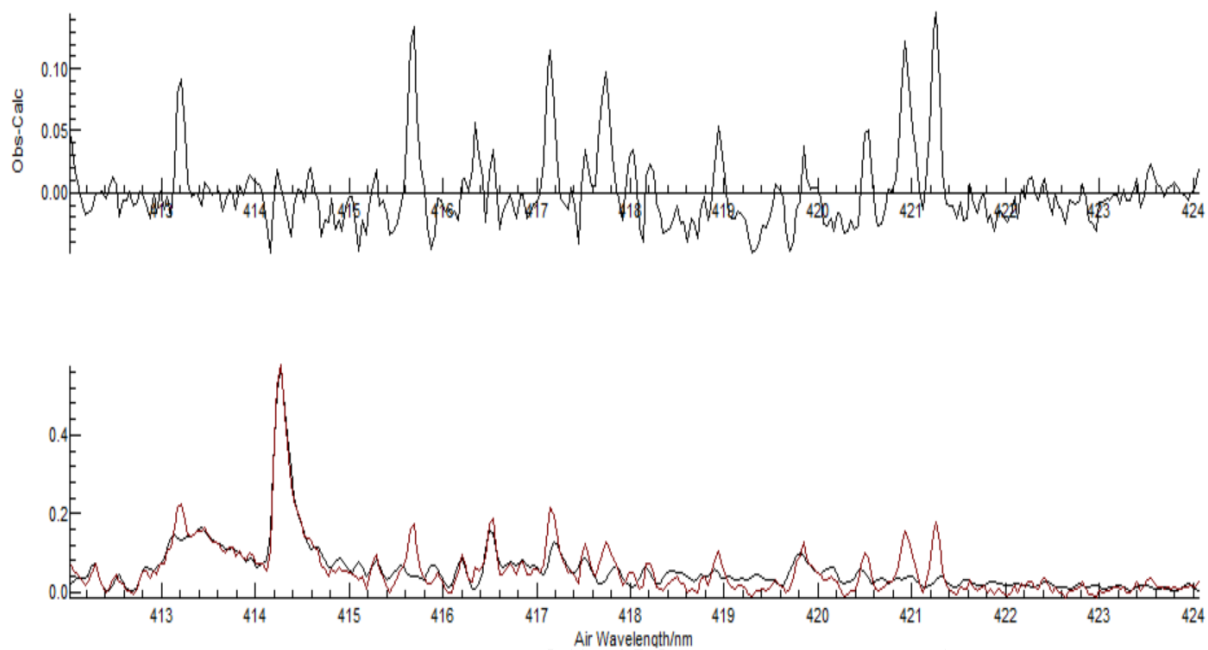


**Figure 3.4: (a) PGOPHER Fit of SiH (A-X) in a SiH<sub>4</sub>/H<sub>2</sub> plasma, corresponding to  $P= 0.9$  kW,  $z = 9.75 \pm 0.75$  mm, (b) Residuals plot. <sup>2</sup>**

### 3.3 SiH<sub>4</sub>/H<sub>2</sub> mixture

The computational processing of the emission spectroscopy data collected led to formation of spatial distributions for each of the species: H\*, Si\* and SiH\*. A spatial distribution or spatial profile is a plot of the relative emission intensity of the species in question, as a function of height above the substrate surface,  $z$ .

For the SiH<sub>4</sub>/H<sub>2</sub> plasma, these spatial distributions were generated as a function of  $F(\text{SiH}_4)$ ,  $P$  and  $p$ , as discussed in Section 2.1.2. In examining these profiles, those generated as a function of  $P$  and  $p$  have been grouped together in the discussion, due to the similar features they share. It is also important to note that H\* has been considered separately to Si\* and SiH\* in all three cases.

### 3.3.1 Spatial distributions for H\*, Si\* and SiH\* as a function of $P$ and as a function of $p$

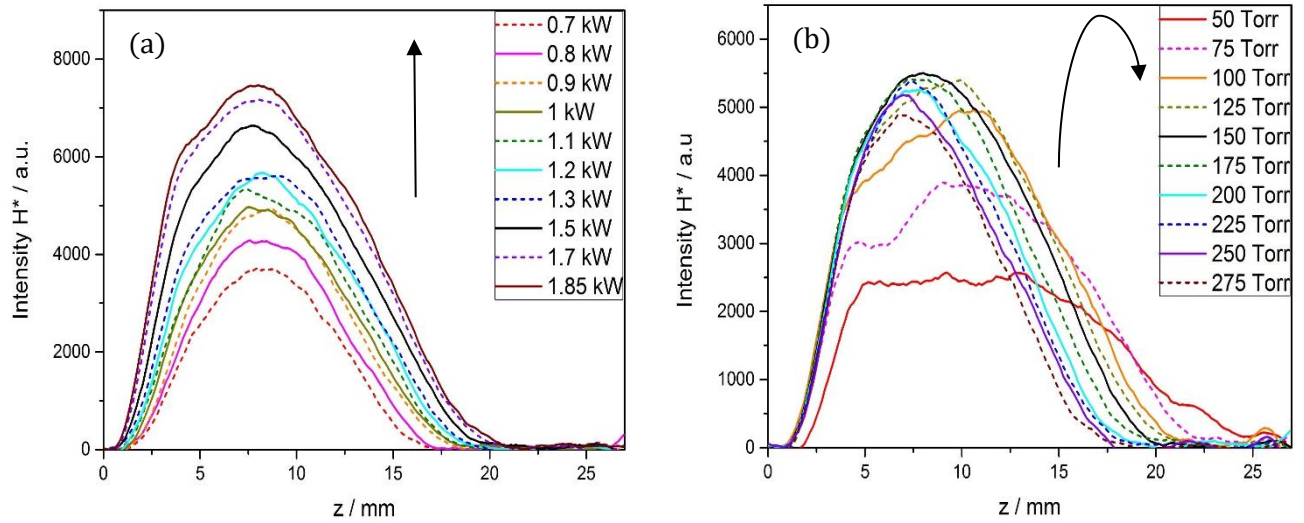


**Figure 3.5: Spatial profiles for H\* in a SiH<sub>4</sub>/H<sub>2</sub> plasma, as a function of: (a)  $P$  and (b)  $p$**

As evident in Figure 3.5 (a),  $I(\text{H}^*)$  has increased with  $P$ , as shown by the diagrammatic arrow on the right of the image. This trend can be explained by the fact that  $T_{\text{gas}}$  increases with power, resulting in greater thermal dissociation of H<sub>2</sub> to atomic H. At the same time, an increase in power causes there to be an increase in ionisation, generating more electrons. As a result, a greater proportion of electrons are involved in electron impact excitation of H to H\*. Therefore, it was a combination of these two effects that resulted in the increase in H\*. A second observation unique to Figure 3.5 (a) was that the  $z$  value associated with peak  $I(\text{H}^*)$  was insensitive to  $P$ . Although peak  $I(\text{H}^*)$  increased with  $P$ , it was associated with  $z \sim 8$  mm for all powers.

With respect to  $p$ , as shown in Figure 3.5 (b), two separate features can be observed in the trend. Firstly, there was a rise in  $I(\text{H}^*)$  as  $p$  was increased to 150 Torr. This trend can be supported by a similar trend observed in a pure H<sub>2</sub> plasma, whereby  $I(\text{H}_\alpha)$  was found to increase with  $p$ <sup>1</sup>. Therefore, the rise in  $I(\text{H}^*)$  observed in Figure 3.5 (b) can be explained. However, beyond  $p = 150$  Torr, although a slight decrease in  $I(\text{H}^*)$  can be observed, the effect at higher  $p$  can be attributed more to a contraction in height rather than a decrease in  $I(\text{H}^*)$ . This differed to the observed spatial profile of H<sub>α</sub> in pure H<sub>2</sub>, under similar conditions. Therefore, this contraction in height could be explained by the presence of silicon in the system. It is possible that on the addition of silicon into the system, the probability of quenching H\* increases, compared to a pure H<sub>2</sub> plasma. Additionally, in a plasma system such as this, an increase in pressure leads to a contraction of the plasma volume. Therefore, beyond  $p = 150$  Torr, this contraction could be explained by the fact that the rate of quenching H\* exceeded the rate of fluorescence, together with the fact that the plasma volume continued to decrease in size.

One final feature observed in both (a) and (b) was the impact that varying  $P$  and  $p$  had respectively on the width of the spatial profiles. An increase in  $P$ , as shown in Figure 3.5 (a), led to an expansion of the spatial profile. However, an increase in  $p$ , Figure 3.5 (b), resulted in a contraction of the profile to lower  $z$ . This particular feature was important with respect to the spatial profiles generated for the  $\text{SiH}_4/\text{H}_2$  plasma, as explained with respect to  $\text{Si}^*$  and  $\text{SiH}^*$  below.

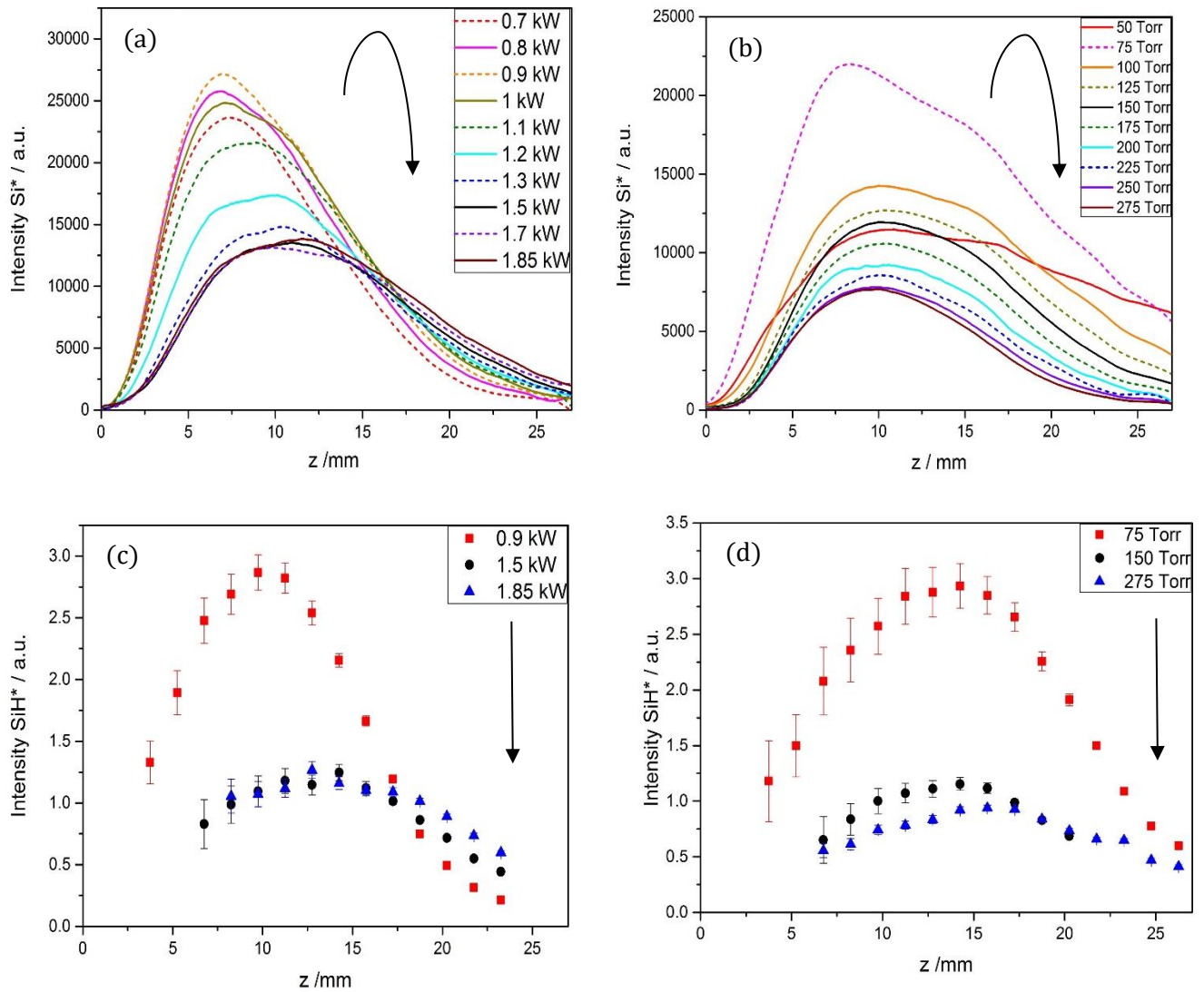


**Figure 3.6: Spatial profiles of  $\text{Si}^*$  in a  $\text{SiH}_4/\text{H}_2$  plasma, as a function of: (a)  $P$  and (b)  $p$ . Also, spatial profiles of  $\text{SiH}^*$  under the same plasma as a function of: (c)  $P$  and (d)  $p$ .**

From the four spatial profiles depicted in Figure 3.6, several key features were observed. Firstly, from comparison of the spatial profile for  $\text{Si}^*$  with that of  $\text{SiH}^*$ , the two were found to have very similar trends, regardless of the parameter being varied. This can be said since the same was observed in the corresponding  $F(\text{SiH}_4)$  spatial profiles, as evident in Section 3.3.2. The main difference between the two was that peak  $I(\text{SiH}^*)$  was observed at a higher  $z$  than the corresponding peak  $I(\text{Si}^*)$ , for all conditions.

Secondly, as shown in Figure 3.6 (a), following an initial modest increase in  $I(\text{Si}^*)$  at low powers,  $I(\text{Si}^*)$  was seen to decrease with increasing  $P$  throughout the region  $P = 0.9$  kW to 1.5 kW. Beyond 1.5 kW,  $I(\text{Si}^*)$  seemingly plateaued. The same trend was seen in the corresponding  $\text{SiH}^*$  spatial profile, Figure 3.6 (c). However, this same trend was also evident in the spatial profiles for  $\text{Si}^*$  and  $\text{SiH}^*$  as a function of  $p$ , Figures 3.6 (b) and (d) respectively. Following a rise in  $I(\text{Si}^*)$  and  $I(\text{SiH}^*)$  at low  $p$ , both of these values decreased with further increases in  $p$ . At this stage, any possible explanations for this trend must necessarily be speculative. One possible explanation for the observed drop in  $I(\text{Si}^*)$  and  $I(\text{SiH}^*)$  values could be an increase in the ionisation of  $\text{Si}^*$  and  $\text{SiH}^*$  species to  $\text{Si}^+$  and  $\text{SiH}^+$  cations. Clustering is another possibility, which might be more readily understandable in the case of increasing  $p$  rather than  $P$ . Any increase in the density of  $\text{SiH}_x$  species and in their frequency of collisions might be expected to encourage their clustering to form  $\text{Si}_n\text{H}_x$  ( $n > 1$ ) species and eventual Si nanoparticle formation.<sup>3</sup> Both of these suggestions would have the net result of reducing  $I(\text{Si}^*)$  and  $I(\text{SiH}^*)$ .

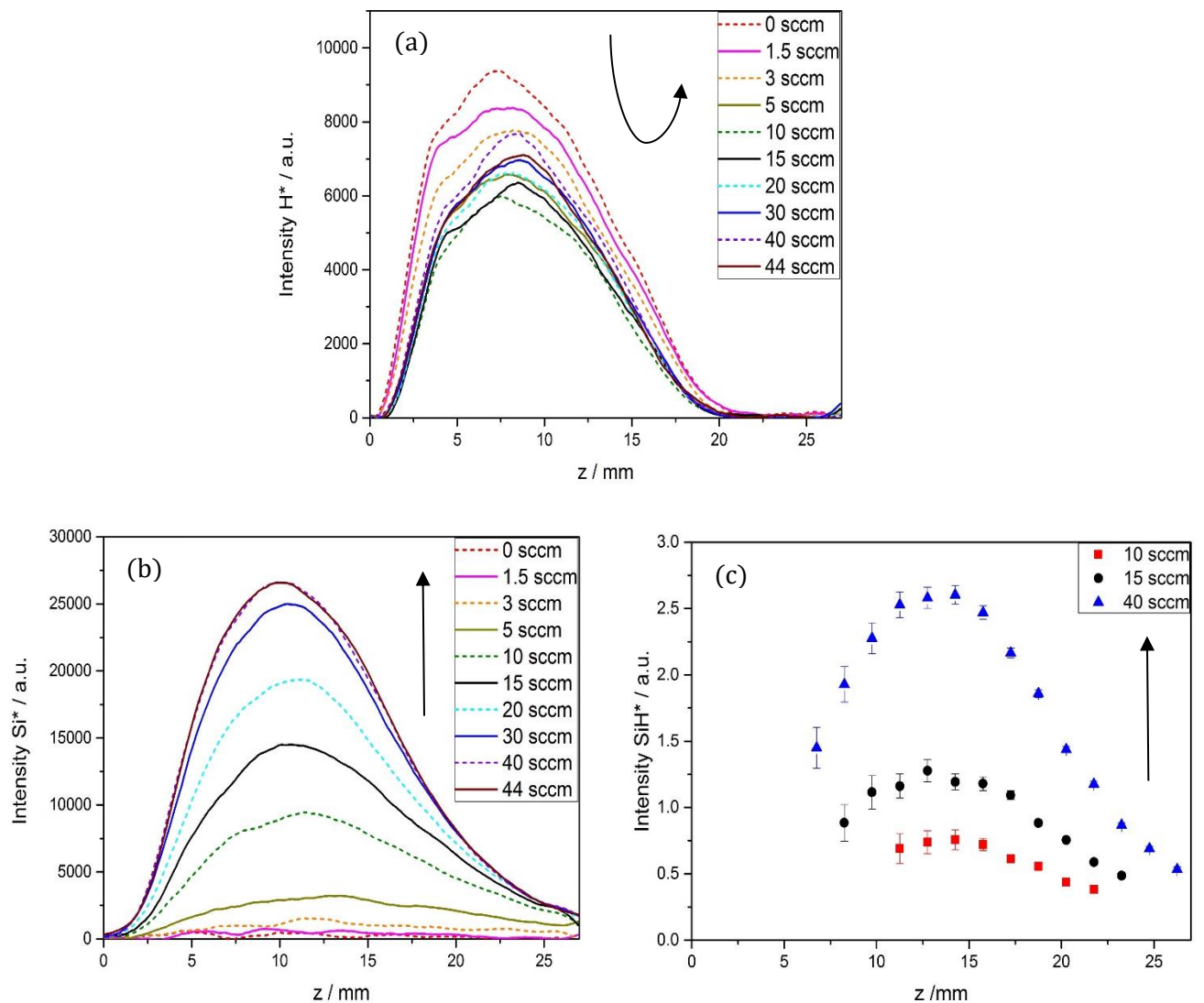
A third key feature observed in Figure 3.6 was that the widths of the  $\text{Si}^*$  and  $\text{SiH}^*$  spatial profiles were affected by  $P$  and  $p$ . The same observation was seen in the corresponding  $\text{H}^*$  spatial profiles, Figure 3.5 (a) and (b). As shown in Figures 3.6 (a) and (c), with increasing  $P$ , the spatial profiles were found to expand to higher  $z$  values. This can be attributed to the power density which remains relatively constant as power is increased. However, in order to maintain the power density, the volume of the plasma must increase with increasing  $P$ . It is for this reason that the spatial profiles expanded to higher  $z$ .<sup>4</sup> In contrast, an increase in  $p$  results in a decrease in the plasma volume. Therefore, as evident in Figures 3.6 (b) and (d), the spatial profiles contracted to lower  $z$  with increasing  $p$ . Overall, it is evident that the width of the spatial profile was dependent on the parameter being varied.

Finally, in both cases,  $I(\text{Si}^*)$  and  $I(\text{SiH}^*)$  were found to extend beyond  $z \sim 27$  mm. As discussed in Section 3.6, the dominant mechanism of forming  $\text{Si}^*$  and  $\text{SiH}^*$  species is expected to be the electron impact excitation of Si and SiH. However, at high  $z$  values, as shown in other studies such as the Ma et al. OES study of a  $\text{CH}_4/\text{H}_2$  plasma, the electron density has been modelled to be very low.<sup>5</sup> Therefore, this suggests two possible conclusions: (i) An alternative mechanism may be responsible for the formation of these species at the periphery of the plasma. In a study conducted by Suto and Lee, emissions for  $\text{Si}^*$  and  $\text{SiH}^*$  were observed following the excitation of  $\text{SiH}_4$ , in the vacuum ultraviolet region (VUV).<sup>6</sup> Therefore, it is possible that a photodissociation type reaction is generating emissions from  $\text{Si}^*$  and  $\text{SiH}^*$  at the periphery of the plasma, explaining why the relative emission intensity values were found to extend beyond  $z \sim 27$  mm. (ii) In the case of the  $\text{SiH}^*$  emission, this could be attributed to a chemiluminescent contribution, similar to the  $\text{BH}^*$

emission observed in the B/H studies.<sup>7</sup> A chemiluminescent contribution of this type would involve the collision and reaction of a silicon atom with a hydrogen atom. These are two potential reasons for the feature observed in both Si\* and SiH\* spatial profiles, however, there is no clear evidence in this study to support either one of them.

### 3.3.2 Spatial distributions for $H^*$ , $Si^*$ and $SiH^*$ as a function of $F(SiH_4)$

The spatial distributions for  $H^*$ ,  $Si^*$  and  $SiH^*$ , as a function of  $F(SiH_4)$ , have been considered separately to those for  $P$  and  $p$ . This is due to the similar features observed in the profiles corresponding to  $P$  and  $p$ , as discussed in Section 3.3.1. The link in their features can be attributed to the fact that the  $SiH_4$  concentration in the reactor was kept constant, with  $F(SiH_4) = 15$  sccm. Different trends were observed in the spatial profiles associated with varying  $F(SiH_4)$ , as expanded on in the following section. It is important to reiterate that  $SiH_4$  refers to a 0.1%  $SiH_4$  in pure  $H_2$  gas mixture. Therefore, a very small content of  $SiH_4$  was present in a very  $H_2$  rich gas mixture.



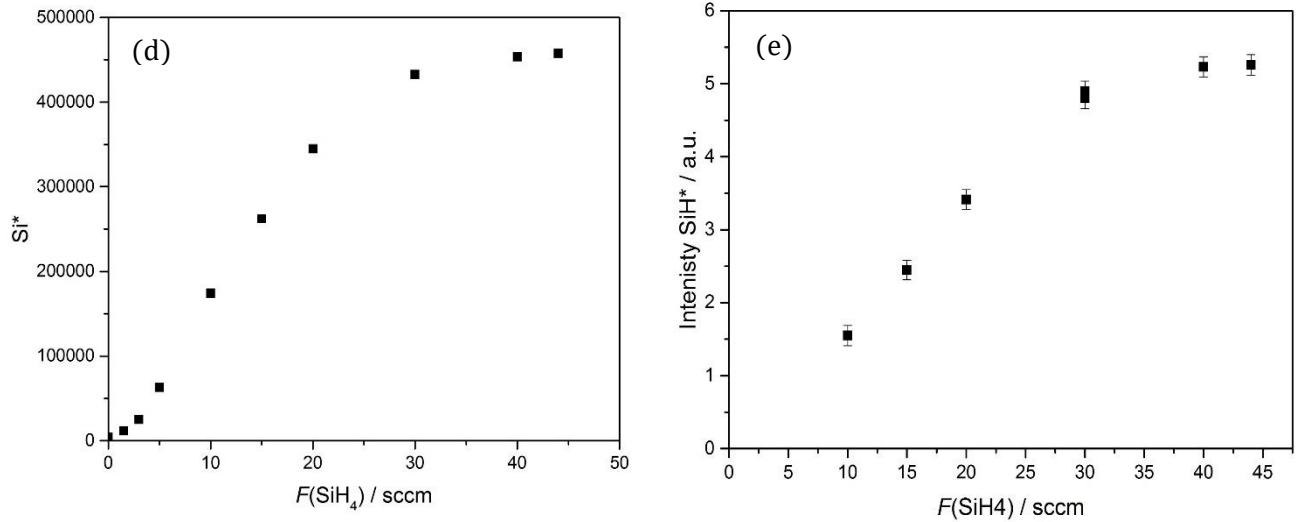


**Figure 10: Spatial profiles for (a) H\*, (b) Si\* and (c) SiH\* as a function of  $F(\text{SiH}_4)$ . Also, presented are plots showing the variation of (d)  $I(\text{Si}^*)$  and (e)  $I(\text{SiH}^*)$  with  $F(\text{SiH}_4)$ , at  $z = 13.5 \pm 1.5$  mm.**

The key observation to highlight with respect to H\* is the decrease in  $I(\text{H}^*)$  from  $F(\text{SiH}_4) = 0$  to 10 sccm. This suggested that at low  $F(\text{SiH}_4)$ , H\* was quenched. A possible reason for this could be that at low  $F(\text{SiH}_4)$ , there was efficient ionisation of the small SiH<sub>4</sub> content present in the mixture. An increase in ionisation results in an increase in electron density,  $n_e$ . However, the electrons produced following ionisation are lower in energy compared to those used for ionisation. This is represented by a decrease in the electron temperature,  $T_e$ . At lower  $T_e$ , the probability of excitation to H\* is lower since fewer electrons have sufficient energy to vibrationally excite H to H\*. Therefore, this increase in SiH<sub>4</sub> ionisation was most likely the cause of this decrease in  $I(\text{H}^*)$ , at low  $F(\text{SiH}_4)$ .

As mentioned earlier, the spatial profiles of Si\* and SiH\*, Figures 3.7 (b) and (c), have evidently followed similar trends. Their respective emission intensities have both increased in magnitude as  $F(\text{SiH}_4)$  has been increased. An additional feature of interest with respect to this increase was the apparent linear relationship between  $I(\text{Si}^*)$  and  $I(\text{SiH}^*)$  with  $F(\text{SiH}_4)$ . This can be seen in Figures 3.7 (d) and (e) respectively. Unlike Figures 3.7 (a) – (c), (d) and (e) are not spatial profiles but show the variation of  $I(\text{Si}^*)$  and  $I(\text{SiH}^*)$  with  $F(\text{SiH}_4)$ , in this case at  $z = 13.5 \pm 1.5$  mm. Each plot shows a linear relationship, until a flow rate between 20 to 30 sccm. The importance of this relationship was significant in determining  $F(\text{SiH}_4) = 15$  sccm as ‘base condition’ for the experiments which followed, involving the variation of  $P$  and of  $p$ . The reason for 15 sccm was due to the fact that it gave the best signal to noise ratio with respect to the emission intensities for the species, as well as the fact that this flow rate value fell in the linear region.

The final observation to note is that the distributions for  $\text{Si}^*$  and  $\text{SiH}^*$  have extended to larger  $z$  values than the corresponding distribution for  $I(\text{H}^*)$ .

### 3.4 Si substrate in the presence of a H<sub>2</sub>/Ar mixture

As discussed in Section 2.1.3, the second system studied was a H<sub>2</sub>/Ar plasma with a Si wafer present. Spatial profiles for H\*, Si\* and SiH\* were plotted as a function of  $F(\text{Ar})$ . In the following discussion of this plasma, two aspects must be considered. Firstly, it is important to consider the role of  $F(\text{Ar})$  and the temperature of the substrate,  $T_{\text{sub}}$ . Following this, the roughness of the Si substrate is discussed, particularly with respect to the corresponding set of spatial profiles produced.

#### 3.4.1 Etching process

As explained in Section 2.1.3, two runs were conducted for each repeat. The first run, involving the initial increase in  $F(\text{Ar})$  from 0 to 300 sccm, is discussed here, with Figure 3.8 showing the corresponding Si\* spatial profile.

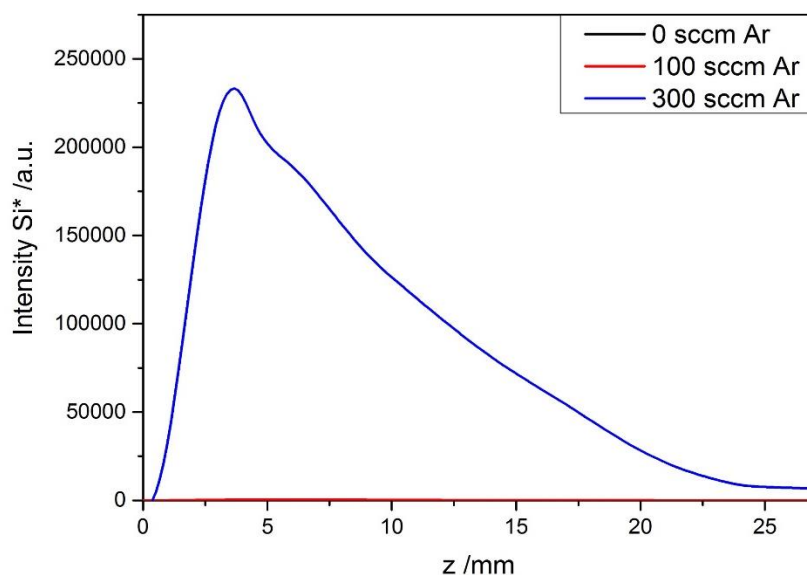


**Figure 3.8: Spatial profile for Si\* as a function of  $F(\text{Ar})$ , in a H<sub>2</sub>/Ar mixture with a Si substrate present. These spatial profiles correspond to the first run.**

In the first run, for  $F(\text{Ar}) = 0$  and 100 sccm, the relative emission intensities for Si\*, as evident in Figure 3.8, and for SiH\* were negligible. However, on increasing  $F(\text{Ar})$  to 300 sccm, it was at this condition that  $I(\text{Si}^*)$  was observed. This can be explained by the presence of argon in the system which had an effect on  $T_{\text{sub}}$ .  $T_{\text{sub}}$  was measured with a 2-color pyrometer (600 – 1300 °C). At the two lower argon flow rates,  $T_{\text{sub}}$  could not be detected by the pyrometer and hence it was determined to be < 600 °C. In contrast, at  $F(\text{Ar}) = 300$  sccm, it was reported as reaching an average  $T_{\text{sub}}$  of 790 °C, with some points reaching temperatures as high as 1117 °C. The

temperature of the substrate was important particularly in the initial run, as it was only at the high temperature that atomic H could etch off the terminated layer of the Si substrate. This layer was believed to be comprised of O and OH termination, since the Si wafer had been exposed to the atmosphere. Once this layer had been etched away, Si from the substrate was exposed, resulting in thermal desorption of this Si into the gas mixture. Following this addition of Si into the gas mixture, species such as Si\* and SiH\* were observed.

### 3.4.2 Spatial distributions for H\*, Si\* and SiH\* as a function of $F(\text{Ar})$

On reaching  $F(\text{Ar}) = 300$  sccm, as discussed in Section 3.4.1, the system was then returned to  $F(\text{Ar}) = 0$  sccm for a period of ten minutes before a second set of OES spectra was obtained. The spatial profiles presented in Figure 3.9 correspond to this second set of data.

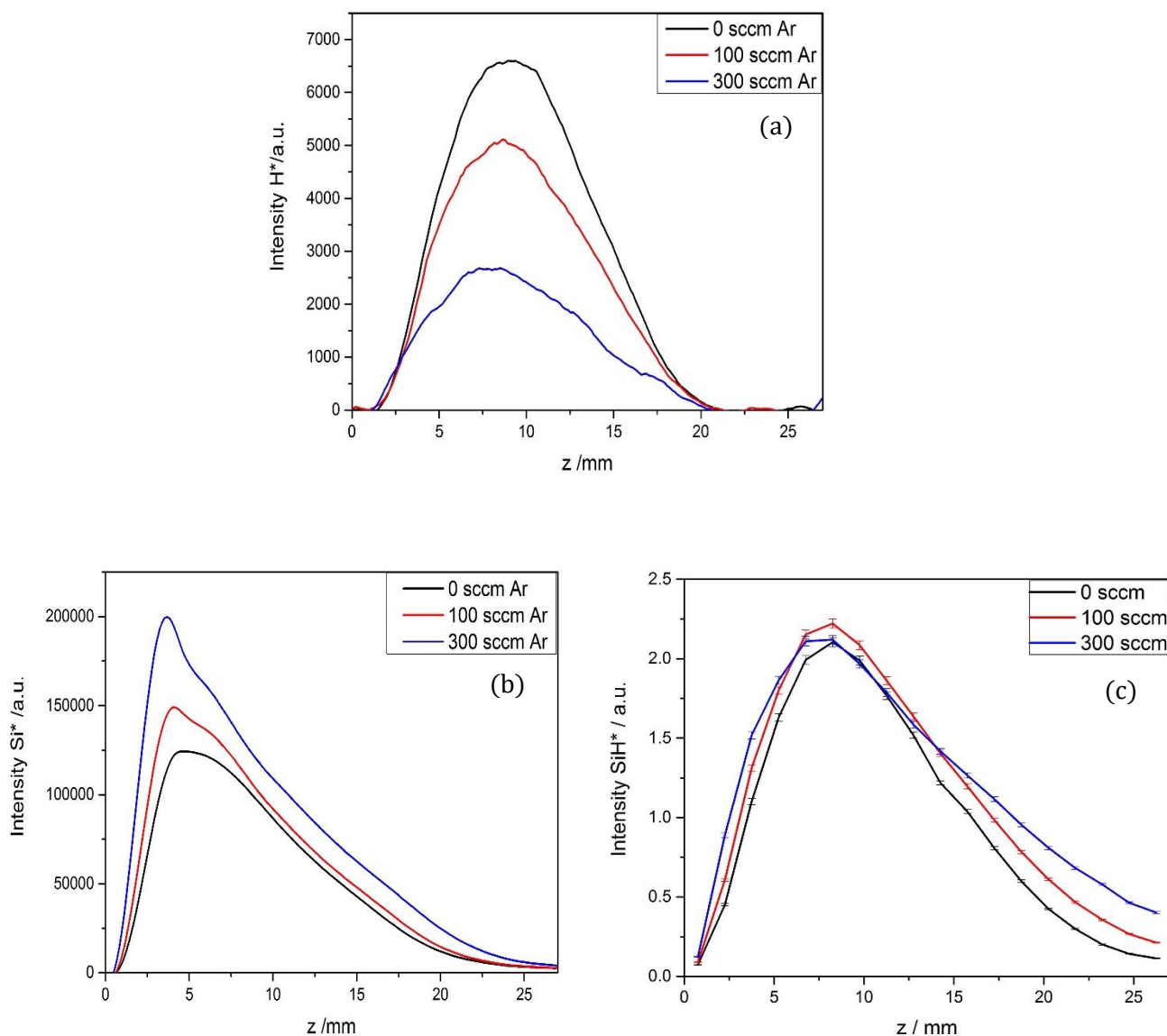


**Figure 3.9: Spatial profiles for (a) H\*, (b) Si\* and (c) SiH\* as a function of  $F(\text{Ar})$ , in a  $\text{H}_2/\text{Ar}$  mixture with a Si substrate present. These spatial profiles correspond to the second run, and hence following the etching of the OH terminated layer.**

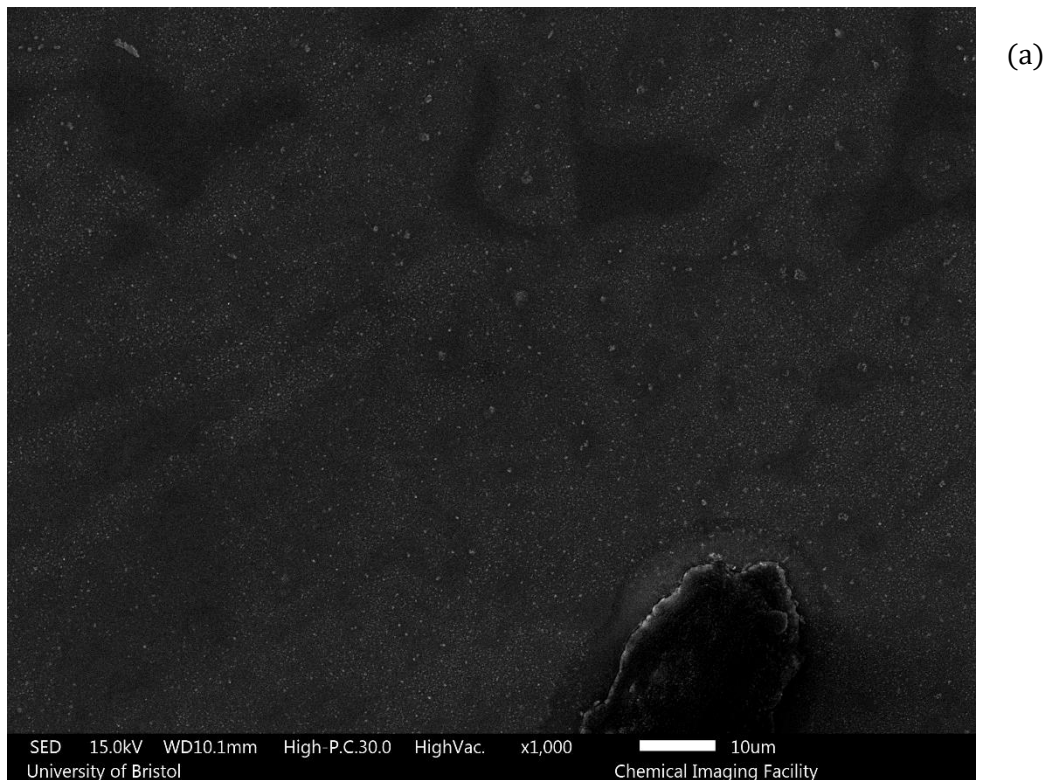
In contrast with the OES data collected for the initial run,  $I(\text{Si}^*)$  and  $I(\text{SiH}^*)$  were observed for  $F(\text{Ar}) = 0$  and 100 sccm, as shown in Figures 3.9 (b) and (c) respectively. The fact that these values were observed provides support for the fact that the O/OH terminated layer must be etched off first, a process which can only occur at a high  $T_{\text{sub}}$ , as discussed in the previous section.

Figure 3.9 (b) shows that as  $F(\text{Ar})$  was increased, there was a very slight shift in peak  $I(\text{Si}^*)$  to lower  $z$ . The profile was also found to expand to higher  $z$ , however,  $I(\text{Si}^*)$  did not extend beyond  $z \sim 25$  mm. On the other hand, as shown in Figure 3.9 (c),  $\text{SiH}^*$  showed some different behaviour. Although there was an expansion of the spatial profile with increasing  $F(\text{Ar})$ ,  $I(\text{SiH}^*)$  was found to extend beyond  $z \sim 27$  mm. This could suggest some type of chemiluminescent contribution to  $\text{SiH}^*$ , similar to the  $\text{SiH}_4/\text{H}_2$  system, as discussed in Section 3.3.1. Alternatively, it is possible that in the substrate system, more silicon is reaching high  $z$ . Another difference between (b) and (c) was the fact that the  $z$  value associated with peak  $I(\text{SiH}^*)$  appeared to be insensitive to  $F(\text{Ar})$ , as it was peak  $I(\text{SiH}^*)$  was observed at approximately the same  $z$  for all three argon flow rates.

With respect to the  $\text{H}^*$  spatial profile shown in Figure 3.9 (a),  $I(\text{H}^*)$  decreased as  $F(\text{Ar})$  rose. Therefore, its behaviour is similar to that observed for  $\text{H}^*$  in a  $\text{H}_2/\text{Ar}$  plasma, in the absence of a Si substrate. <sup>1</sup>

### 3.4.3 SEM

The second aspect to consider with respect to this particular system is the type of Si substrate used. As explained in Section 2.1.3, the procedure was first carried out with a smooth Si wafer. The procedure was then repeated with the same (now rougher) wafer, having already been exposed to the plasma, as shown in Figure 2.6. As discussed in Section 2.4, SEM was used to determine the difference in the surface topographies of the Si wafer at different stages of the experiment. Figure 3.10 shows SEM images taken from each substrate, at a magnification of x 1000.



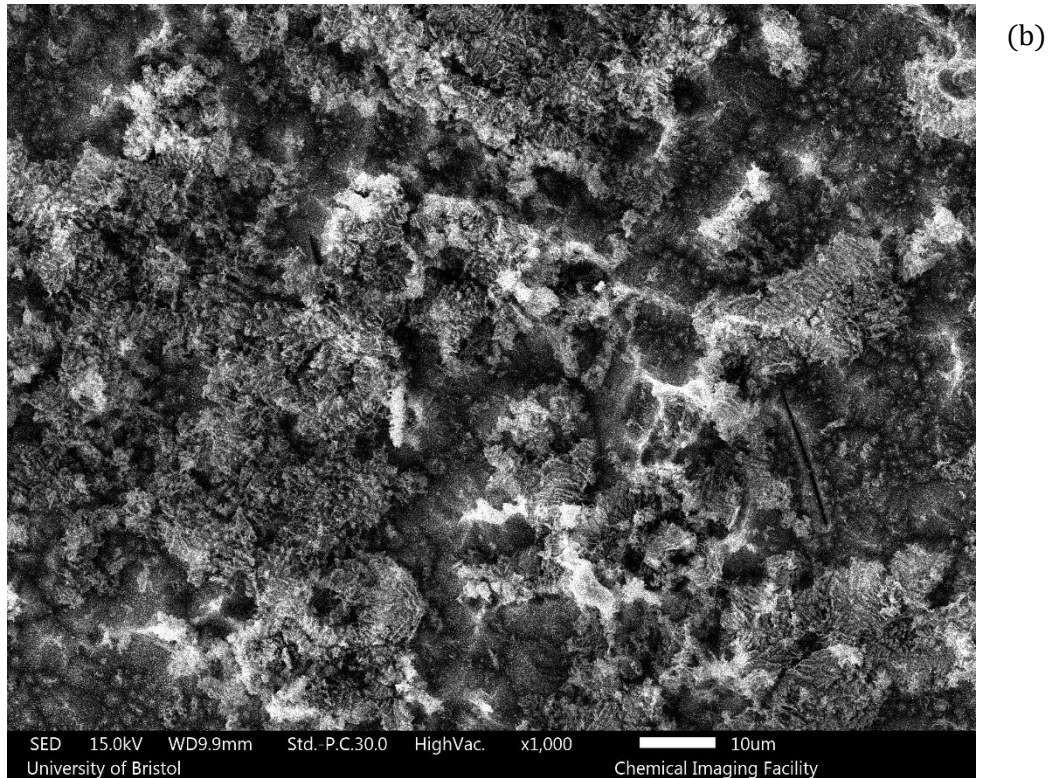


**Figure 3.10: Representative SED type SEM images of the (a) Clean, unexposed Si wafer and (b) Si wafer having been exposed to a H<sub>2</sub>/Ar plasma. Both images were taken at a magnification of x1000.**

By comparing Figure 3.10 (a) with (b), it is evident that on exposure to the H<sub>2</sub>/Ar plasma, the Si substrate became rougher. As discussed in Section 3.4.1, etching of the silicon wafer was only enabled on exposure to a 50% Ar/H<sub>2</sub> plasma. This was verified in the two repeats of the experiment, irrespective of their differing surface morphologies. In addition, the spatial distributions generated in both repeats were found to be essentially identical. Therefore, this suggests that initial roughness of the Si wafer had no evident impact on the gas phase chemistry. However, in order to remove the terminated surface layer of the Si wafer, the substrate needed to reach high temperatures.

### 3.5 Comparison of spatial distributions for $I(\text{H}^*)$ , $I(\text{Si}^*)$ and $I(\text{SiH}^*)$ from a Si wafer in a pure $\text{H}_2$ plasma and those from a $\text{SiH}_4/\text{H}_2$

The purpose of the following discussion is to compare the spatial distributions obtained from the two different sources of silicon. These are shown in Figure 3.11. The spatial distributions shown in black were obtained from the  $\text{SiH}_4/\text{H}_2$  plasma, a system involving a gas phase source of silicon. These particular profiles were obtained using base conditions of  $F(\text{H}_2) = 300$  sccm  $F(\text{SiH}_4) = 15$  sccm,  $P = 1.5$  kW and  $p = 150$  Torr. In contrast, the spatial distributions shown in blue correspond to the Si substrate in a pure  $\text{H}_2$  plasma, under the same base conditions for  $F(\text{H}_2)$ ,  $P$  and  $p$ .

It is important to note that the spatial distributions, in Figure 3.11, have been normalised to allow for comparison of the different profiles from the plasma and substrate. For this reason, the left and right  $y$ -axis intensity scales differ.

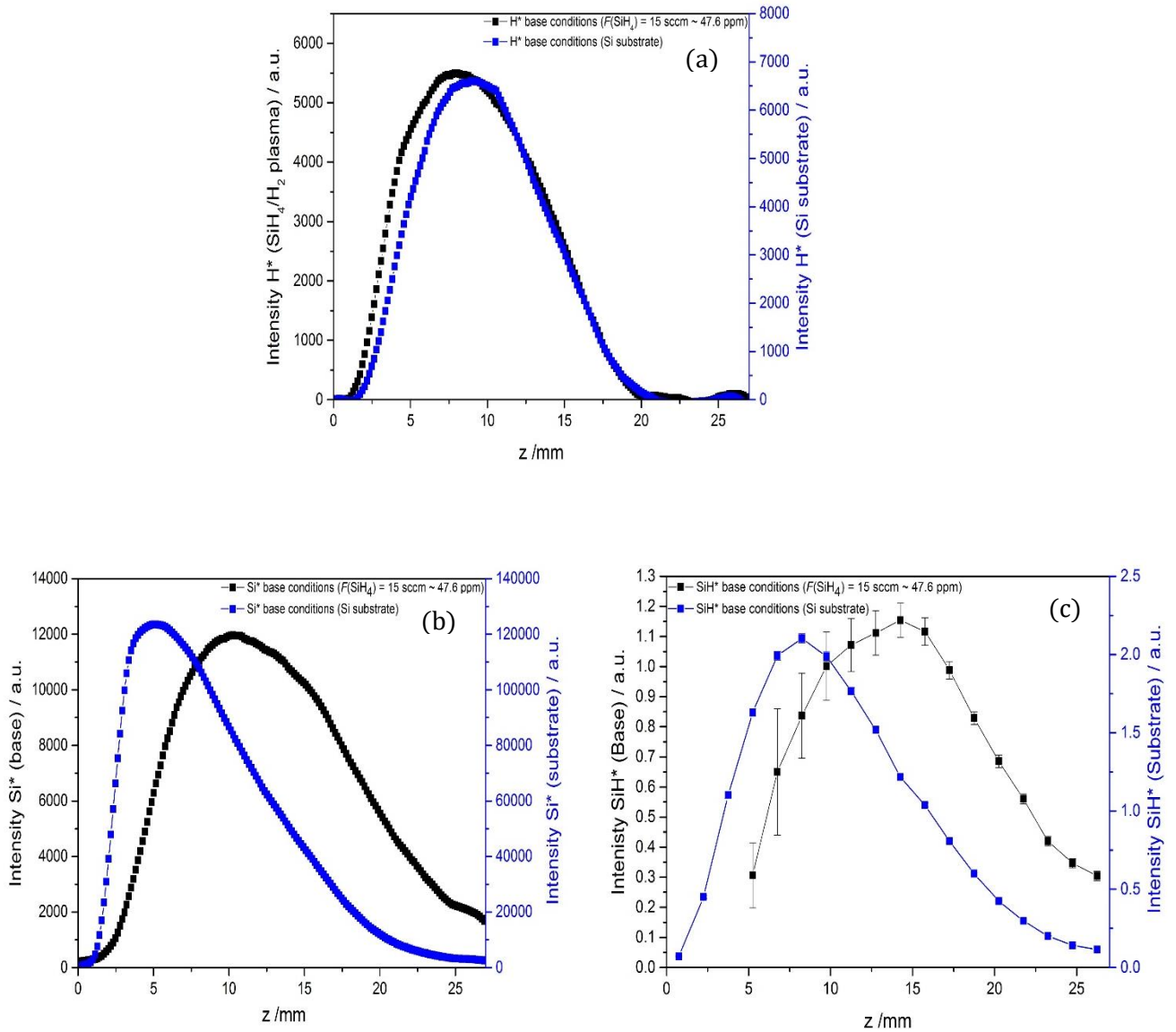


**Figure 3.11 : Comparison of spatial profiles for (a)  $\text{H}^*$ , (b)  $\text{Si}^*$  and (c)  $\text{SiH}^*$  from a Si wafer in a pure  $\text{H}_2$  plasma (blue) and that arising from a  $\text{SiH}_4/\text{H}_2$  plasma operating at base conditions (black)**

As shown in Figure 3.11 (a), the two distributions for  $\text{H}^*$  were found to be very similar. Therefore, this suggested that the nature of the silicon source had no significant impact on  $\text{H}^*$ . The one key difference between the two was the width of their spatial profiles, with a broader  $\text{H}^*$  distribution for the  $\text{SiH}_4/\text{H}_2$  plasma.

In contrast,  $\text{Si}^*$  and  $\text{SiH}^*$  spatial profiles were clearly different in the two systems, as shown in Figures 3.11 (b) and (c). Peak  $I(\text{Si}^*)$  and  $I(\text{SiH}^*)$  for the substrate system appeared at lower  $z$  than those for plasma. This can be explained if we consider the nature of the two different silicon sources and the incorporation of silicon into the gas mixture. For the substrate, silicon was introduced through thermal desorption of the wafer surface. Therefore,  $\text{Si}^*$  and  $\text{SiH}^*$  should be expected to be present at low  $z$ , closer to the surface. For the  $\text{SiH}_4/\text{H}_2$  system,  $\text{SiH}_4$  was fed into the reactor through the gas inlet, at higher  $z$ . For this reason,  $\text{Si}^*$  and  $\text{SiH}^*$  were found at relatively higher  $z$  values compared to the substrate.

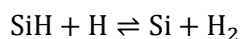
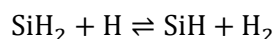
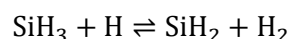
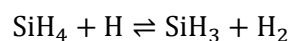
A second feature observed was that the spatial profiles for  $\text{Si}^*$  and  $\text{SiH}^*$  in the  $\text{SiH}_4/\text{H}_2$  plasma were broader than those associated with the substrate. As mentioned earlier, this same feature was observed with respect to the  $\text{H}^*$  spatial profiles in (a). A possible reason for this could be the fact the electron impact excitation makes a greater contribution to the total  $I(\text{Si}^*)$  emission in the absence of  $\text{SiH}_4$ .

## 3.6 Gas phase chemistry

Overall, this study has provided evidence for the presence of Si\* and SiH\* species in two different silicon-containing hydrogen plasmas. There are several potential mechanisms for the formation of these excited state species, such as photodissociation and chemiluminescent reactions, as discussed in Section 3.3.1. However, the primary mechanism is believed to have been electron impact excitation, as shown in Reactions 3.1 and 3.2. Following collision with an electron, the SiH<sub>x</sub> species was vibrationally excited to SiH<sub>x</sub><sup>\*</sup>, Reaction 3.1. This excited species then relaxed back to its ground state, releasing a photon of energy in the process, Reaction 3.2. This characteristic photon energy corresponded to the emission observed in the OES spectrum.



As Reactions 3.1 and 3.2 show, in order to form Si\* and SiH\*, atomic Si and SiH were needed respectively. With respect to the SiH<sub>4</sub>/H<sub>2</sub> system, evidence for the presence of Si and SiH in the gas mixture was significant in determining Scheme 3.1, a set of reactions put forward for the silicon based gas phase chemistry occurring in the reactor. As discussed before, SiH<sub>4</sub> was present in a relatively low concentration, with  $F(\text{SiH}_4)$  corresponding to ~ 47.6 ppm of SiH<sub>4</sub> in H<sub>2</sub>. Also, as evident from the presence of H\*, this indicated the presence of atomic H in the gas mixture. Therefore, with SiH<sub>4</sub> as the sole source of silicon, in the presence of a large concentration of atomic H, a set of hydrogen abstractions were believed to be key to the generation of SiH<sub>x</sub> species such as Si and SiH.



### Scheme 3.1: Proposed set of gas phase reactions for the SiH<sub>4</sub>/H<sub>2</sub> plasma

It is important to highlight that Scheme 3.1 is a **proposed** set of reactions to explain the silicon gas phase chemistry. It has been put forward based on the observations from the features observed in this qualitative OES study, together with considering a similar CH<sub>4</sub>/H<sub>2</sub> system, as discussed in Section 1.3.<sup>8</sup>

### 3.7References

- 1) E. J. D. Mahoney, S. Mushtaq, M. N. R. Ashfold, and Yu. A. Mankelevich, 'Spatially Resolved Optical Emission and Modelling Studies of Microwave-Activated H<sub>2</sub> Plasmas Operating under Conditions Relevant for Diamond Chemical Vapor Deposition', awaiting submission to *J. Phys. Chem. A*
- 2) PGOPHER, A Program for Simulating Rotational, Vibrational and Electronic Spectra, C. M. Western, University of Bristol, <http://pgopher.chm.bris.ac.uk>
- 3) B. Barwe, F. Riedel, O. E. Cibulka, I. Pelant and J. Benedikt, *J. Phys. D*, 2015, **48**, 314001.
- 4) Y. A. Mankelevich, M. N. R. Ashfold and J. Ma, *J. Appl. Phys.*, 2008, **104**, 113304.
- 5) J. Ma, M. N. R. Ashfold and Y. A. Mankelevich, *J. Appl. Phys.*, 2009, **105**, 043302.
- 6) M. Suto and L. C. Lee, *J. Chem. Phys.*, 1986, **84**, 1160-1164.
- 7) J. Ma, J. C. Richley, D. R. W. Davies, A. Cheesman, M. N. R. Ashfold and Y. A. Mankelevich, *J. Phys. Chem. A*, 2010, **114**, 2447-2463.
- 8) J. E. Butler, Y. A. Mankelevich, A. Cheesman, J. Ma and M. N. R. Ashfold, *J. Phys. Condens. Matter*, 2009, **21**, 364021.

## 4. Conclusion

Overall, there are several conclusions that can be drawn from the study reported here. Firstly, it is evident that  $H^*$ ,  $Si^*$  and  $SiH^*$  were prominent species in the core of the silicon containing hydrogen plasmas studied. From their presence, ideas can be generated about the gas phase chemistry taking place in such systems, such as the set of reactions proposed in Section 3.6.

Secondly, regardless of the silicon source, the same species were observed. Additionally, as discussed in Section 3.5, the spatial profiles were similar for both systems at base conditions. The difference between the two was that peak  $I(Si^*)$  and  $I(SiH^*)$  were observed at lower  $z$  values for the Si substrate. However, this difference can simply be attributed to the position of the silicon source relative to the Mo substrate surface, as discussed in Section 3.5.

Thirdly, with respect to the  $H_2/Ar$  system studied, it was observed that silicon could only be incorporated into the gas phase once the OH terminated layer had been etched off, a process which occurred at high  $T_{sub}$  values. Additionally, as confirmed by SEM, the initial roughness of the Si wafer seems to have had no apparent impact on the gas phase chemistry.

## 5. Future Work

### 5.1 Modelling of the silicon-containing hydrogen plasmas

Although several pieces of information can be drawn from this study, as discussed in Section 4, OES studies alone are not sufficient evidence for proposed ideas about the gas phase chemistry of any system. For this reason, an OES study such as this is often coupled with 2-D (r,z) plasma chemical modelling. With respect to the studies conducted by Bristol University, this type of modelling is conducted by a team of collaborators in Moscow.

In the past, this team has generated models for a range of microwave activated mixtures. These have included CH<sub>4</sub>/H<sub>2</sub>/Ar<sup>1</sup>, as well as other CH<sub>4</sub>/H<sub>2</sub> and H<sub>2</sub> systems involving the addition of B<sub>2</sub>H<sub>6</sub>,<sup>2,3</sup> N<sub>2</sub><sup>4,5</sup> and CO<sub>2</sub><sup>6,7</sup>. The extensive list highlights the point that modelling is integral to understanding these systems.

Therefore, it is important to compare the features observed in this study with 2D (r,z) chemical models of the two silicon-containing hydrogen plasmas. These models should help to identify the prominent species expected in the core of the plasmas, as well as to predict how these species are impacted by the same process conditions varied in the study reported in this thesis. In this way, the accuracy of the observations and features reported in this study should be determined. At the time of writing, modelling is already underway.

### 5.2 Cavity Ring Down Spectroscopy Study

It is important to note that this OES study provides only qualitative information. The spatial distributions are associated with relative emission intensities of the species. To add to the understanding of the Si/H system, it would be beneficial to gain some quantitative footing. This cannot be done through an emission study but can be done through an absorption study such as Cavity Ring Down Spectroscopy, CRDS.

CRDS studies have been conducted in the past, such as in the study of the CH<sub>4</sub>/H<sub>2</sub>/Ar mixture<sup>8</sup> mentioned in Section 5.1. This technique was used to measure absolute column densities of C<sub>2</sub> and CH, as a function of z. Through comparison of these values with predicted absolute column densities, the measured values were found to be very similar. As a result, this suggested that the predicted column densities for other abundant radicals in the CH<sub>4</sub>/H<sub>2</sub>/Ar system were relatively accurate.<sup>8</sup>

With respect to the Si/H system, CRDS could be used to measure absolute column densities of ground state Si atoms. This is a study that should hopefully be conducted by the Bristol CVD diamond group later on this year.

### 5.3 An OES study of a CH<sub>4</sub>/SiH<sub>4</sub>/H<sub>2</sub> plasma

With a better understanding of the Si/H plasma, the next step is to incorporate CH<sub>4</sub> into the input gas mixture. It is important to highlight that study into microwave-activated silicon-containing hydrogen plasmas is driven by the interest in silicon doped diamond, as discussed in Section 1.4.

Therefore, the next step should be to add CH<sub>4</sub> to the reactor and to conduct a similar OES experiment. Small silicon and carbon containing species should be observed. Species such as Si, SiH, CH and C<sub>2</sub> should be looked for in particular, due to their presence in Si/H and C/H plasmas respectively. However, depending on the nature of the gas phase chemistry of the Si/C/H system, it is possible that these may not be detected. For the species observed by OES, spatial distributions should be generated as a function of  $F(\text{CH}_4)$ ,  $F(\text{SiH}_4)$ ,  $P$  and  $p$ . A study of this type will hopefully be conducted by the Bristol CVD diamond group at some point in the next year or so.

### 5.4 References

- 1) Y. A. Mankelevich, M. N. R. Ashfold and J. Ma, *J. Appl. Phys.*, 2008, **104**, 113304.
- 2) J. Ma, J. C. Richley, D. R. W. Davies, M. N. R. Ashfold and Y. A. Mankelevich, *J. Phys. Chem. A*, 2010, **114**, 10076-10089.
- 3) J. Ma, J. C. Richley, D. R. W. Davies, A. Cheesman, M. N. R. Ashfold and Y. A. Mankelevich, *J. Phys. Chem. A*, 2010, **114**, 2447-2463.
- 4) B. S. Truscott, M. W. Kelly, K. J. Potter, M. Johnson, M. N. R. Ashfold and Y. A. Mankelevich, *J. Phys. Chem. A*, 2015, **119**, 12962-12976.
- 5) B. S. Truscott, M. W. Kelly, K. J. Potter, M. Johnson, M. N. R. Ashfold and Y. A. Mankelevich, *J. Phys. Chem. A*, 2015, **119**, 129260-12976.
- 6) M. W. Kelly, J. C. Richley, C. M. Western, M. N. R. Ashfold and Y. A. Mankelevich, *J. Phys. Chem. A*, 2012, **116**, 9431-9446.
- 7) J. C. Richley, M. W. Kelly, M. N. R. Ashfold and Y. A. Mankelevich, *J. Phys. Chem. A*, 2012, **116**, 9447-9458.
- 8) J. Ma, J. C. Richley, M. N. R. Ashfold and Y. A. Mankelevich, *J. Appl. Phys.*, 2008, **104**, 103305.